

## MASTER'S THESIS

### Synthesis and characterization of Prussian red derived microparticles for the heterogeneous photo-fenton oxidation of azo-type textile dyes as pollutants

Lai, Joshua

*Date of Award:*  
2020

[Link to publication](#)

#### General rights

Copyright and intellectual property rights for the publications made accessible in HKBU Scholars are retained by the authors and/or other copyright owners. In addition to the restrictions prescribed by the Copyright Ordinance of Hong Kong, all users and readers must also observe the following terms of use:

- Users may download and print one copy of any publication from HKBU Scholars for the purpose of private study or research
- Users cannot further distribute the material or use it for any profit-making activity or commercial gain
- To share publications in HKBU Scholars with others, users are welcome to freely distribute the permanent URL assigned to the publication

**HONG KONG BAPTIST UNIVERSITY**

**Master of Philosophy**

**THESIS ACCEPTANCE**

DATE: October 29, 2020

STUDENT'S NAME: LAI Joshua

THESIS TITLE: Synthesis and Characterization of Prussian Red Derived Microparticles for the Heterogeneous Photo-Fenton Oxidation of Azo-type Textile Dyes as Pollutants

This is to certify that the above student's thesis has been examined by the following panel members and has received full approval for acceptance in partial fulfilment of the requirements for the degree of Master of Philosophy.

Chairman: Dr Tong Tiejun  
Associate Professor, Department of Mathematics, HKBU  
(Designated by Dean of Faculty of Science)

Internal Members: Prof Wong Ricky M S  
Professor, Department of Chemistry, HKBU  
(Designated by Head of Department of Chemistry)

Dr Leung Ken C F  
Associate Professor, Department of Chemistry, HKBU

External Examiner: Dr Wong Man-kin  
Associate Professor  
Department of Applied Biology & Chemical Technology  
The Hong Kong Polytechnic University

Issued by Graduate School, HKBU

**Synthesis and Characterization of Prussian Red Derived  
Microparticles for the Heterogeneous Photo-Fenton Oxidation of  
Azo-type Textile Dyes as Pollutants**

**LAI Joshua**

**A thesis submitted in partial fulfilment of the requirements  
for the degree of  
Master of Philosophy**

**Principal Supervisor:**

**Dr. LEUNG Ken C F (Hong Kong Baptist University)**

**October 2020**

## DECLARATION

I hereby declare that this thesis represents my own work which has been done after registration for the degree of MPhil at Hong Kong Baptist University, and has not been previously included in a thesis or dissertation submitted to this or any other institution for a degree, diploma or other qualifications.

I have read the University's current research ethics guidelines, and accept responsibility for the conduct of the procedures in accordance with the University's Research Ethics Committee (REC). I have attempted to identify all the risks related to this research that may arise in conducting this research, obtained the relevant ethical and/or safety approval (where applicable), and acknowledged my obligations and the rights of the participants.

Signature: \_\_\_\_\_   
Date: October 2020

## Abstract

Inorganic colloidal synthesis, without a doubt, lies at the foundation of many contemporary areas of nanoscience and nanotechnology. At the advent of the 21<sup>st</sup> century, much progress has been made in the size, shape / morphological control and surface engineering of metal oxides resulting in a diverse library of macroscopic crystal architectures with well-defined surface properties. In this thesis, we start by introducing the self-assembly of the iron(oxy-, hydro-)xide while briefly reviewing some fundamental concepts of solid-state chemistry. Specific information on the family of iron oxide and iron(oxy-, hydro-)xide, as relevant to crystalline phase control, has been highlighted to direct our discussion of the synthesis of diverse crystal morphologies. Furthermore, we briefly underline and discuss the kinetic and thermodynamic control of colloidal crystal morphologies through reasonably established knowledge of anisotropic growth rates in the perspective of iron oxides' facets or crystalline planes. Lastly, we review the state-of-the-art wet chemical synthetic approaches, while using different iron(oxy-, hydro-)xide crystals as examples, for the purpose of explaining our synthetic work of choice.

The main work of this thesis is entirely focused on the “facile synthesis and fine morphological tuning of branched hematite ( $\alpha$ -Fe<sub>2</sub>O<sub>3</sub>) crystals for photodegradation of azo-type dyes”. We would discuss the crucial parameters for fine morphological tuning in the context of controlling the anisotropic growth rates of branched  $\alpha$ -Fe<sub>2</sub>O<sub>3</sub> crystals instead of phase transformation. In our work, we have significantly improved the synthesis of dendritic “*feather-like*” and “*starfish-like*” for their size reduced variants for use in photocatalysis.

## Acknowledgement

Firstly, I would like to express my gratitude towards my supervisor, Dr. Ken Cham-Fai Leung, for his kindness, patience, and generosity, not for me exclusively, but the entire research group as well. Secondly, I would like to thank Dr. Shou-Hu Xuan, Dr. Yuen-Kit Cheng, and Dr. Xunjin Zhu for their invaluable advice and insights in the devising of crucial experimental ideas and concepts of this research. Moreover, I am grateful for Dr. Xuan Li, Dr. Ruitao Zhou, and Dr. Govardhana Babu Bodedla as their sharing of personal experiences in the laboratory have broadened my horizon in what it means to conduct contemporary research using wet chemistry techniques in the modern context.

Certainly, this project would not have been possible without Dr. Kwan Chak-Shing, Ms. Yung Wing-Yin, and Mr. Tang Fung-Kit, my former colleagues, for their conversations, encouragements, and group discussions despite being pre-occupied with their own research projects. Their determination, dedication and discipline towards research are infectious in a positive light. With the core emphasis in understanding fundamental knowledge, I am delighted to study with Mr. Li Wai-Chung as his knowledge and experience in the mechanisms of particle synthesis has provided me insights in the nucleation and growth of my own colloidal particles.

Overall, I am blessed to have such understanding and accommodating mentors, seniors and colleagues around me in Hong Kong, my home and birthplace.

Finally, I would like to show utmost appreciation to my dear parents as they have always prioritized me and my brothers' education, safety, and overall well-being above all else throughout my lifetime. This academic journey would not have been possible without them. Thank you!

# Table of Contents

<b>Declaration</b> .....	i
<b>Abstract</b> .....	ii
<b>Acknowledgement</b> .....	iii
<b>Table of Content</b> .....	iv
<b>List of Tables &amp; Figures</b> .....	v
<b>Chapter 1: Introduction</b> .....	1
1.1 Background of Crystal Structure .....	1
1.2 Morphological Control of Crystals.....	7
1.3 Wet Chemical Synthetic Methods .....	10
1.4 Chemistry of Fenton Oxidation.....	11
1.5 Expected Findings of Study .....	13
1.6 Outline of the Thesis.....	13
<b>Chapter 2: Facile Synthesis &amp; Fine Morphological Tuning of Branched Hematite (<math>\alpha</math>-Fe<sub>2</sub>O<sub>3</sub>) Crystals for Photodegradation of Azo-Type Dyes</b> .....	15
2.1 Introduction .....	15
2.2 Results & Discussion.....	16
2.3 Experimental Procedure.....	54
2.4 Summary & Future Work.....	59
<b>List of References</b> .....	60
<b>Curriculum Vitae</b> .....	65

## List of Tables and Figures

<b>Table 1.1</b> Summary and categorization of the Bravais lattices to the respective point groups, crystal systems and families.....	P.2
<b>Figure 1.1</b> Schematic representation of the formation process of ferrous hydroxide, termed Fe(OH) <sub>2</sub> , isostructural to brucite.....	P.4
<b>Figure 1.2</b> Transformation pathways of akageneite ( $\beta$ -FeOOH) and goethite ( $\alpha$ -FeOOH) via dissolution-recrystallization of thermodynamic unstable ferrihydrite.....	P.6
<b>Figure 1.3</b> Images of single-crystalline hematite morphology obtained using different capping agents.....	P.9
<b>Figure 1.4</b> Schematic representation showing the “step-by-step” mechanisms of epitaxial growth in the example of SnO <sub>2</sub> nanorods growing on $\alpha$ -Fe <sub>2</sub> O <sub>3</sub> substrates.....	P.11
<b>Figure 2.1</b> Synthetic scheme of various dendritic-shaped $\alpha$ -Fe <sub>2</sub> O <sub>3</sub> fractal structures via a solvothermal reaction in bi-solvent medium.....	P.19
<b>Figure 2.2 (A-J)</b> Low & <b>(K-O)</b> high magnification FE-SEM images of $\alpha$ -Fe <sub>2</sub> O <sub>3</sub> fractal structures synthesized with a typical K <sub>3</sub> [Fe(CN) <sub>6</sub> ] concentration of 4 mM at 180°C for 20 h.....	P.20
<b>Figure 2.3 (A-E)</b> Size and <b>(F-J)</b> angle distribution data of <b>(A,F)</b> secB3D, <b>(B,G)</b> tertD2D, <b>(C,H)</b> tertD3D, <b>(D,I)</b> secS2D and <b>(E,J)</b> hypB2D with a sample size of N = 300.....	P.21
<b>Figure 2.4 (A)</b> Low and <b>(B)</b> high magnification TEM images of an unusual tertD2D particle in the micron and submicron scales, respectively.....	P.22
<b>Figure 2.5</b> Low magnification <b>(A-B)</b> FE-SEM and <b>(C-D)</b> TEM images, showing the <b>(A,C)</b> “back” and <b>(B,D)</b> “front” sides of typical tertD3D particles, respectively.....	P.24
<b>Figure 2.6 (A,C)</b> Low and <b>(B,D)</b> high magnification TEM images of typical secS2D particles showing a <b>(A)</b> normal and <b>(C)</b> stacked variant, respectively, in the submicron scale.....	P.32
<b>Figure 2.7 (A)</b> Low and <b>(B)</b> high magnification FE-SEM images of typical hypB2D particles (as major product) in H <sub>2</sub> O:EtOH bi-solvent ratio of 1 : 3 at the micron scale.....	P.32

**Figure 2.8** pXRD patterns of secB3D (purple), tertD2D (green), tertD3D (blue), secS2D (red) and hypB2D (black), matching closely to that of pure  $\alpha$ -Fe<sub>2</sub>O<sub>3</sub> phase (JCPDS 33-0664).....P.35

**Figure 2.9** FTIR spectra of the (A) as synthesized dendritic microparticles, namely secB3D (ocean blue), tertD2D (orange), tertD3D (grey), secS2D (yellow) and hypB2D (sky blue), and (B) secS2D before (blue) and after calcination (orange) from 40 to 900°C (40°C/min). .....P.36

**Figure 2.10** TGA diagram of secS2D showing the onset (X1, Y1) and offset (X2, Y2) points of a thermal transition curve, which ranges from the initial temperature at 40 to 260°C...P.37

**Figure 2.11** (a) Low and (b) high magnification FE-SEM images of branched  $\alpha$ -Fe<sub>2</sub>O<sub>3</sub> fractals synthesized with a K<sub>3</sub>[Fe(CN)<sub>6</sub>] concentration of 38 mM at 180°C for 20 h. (c) pXRD pattern of the sample confirming formation of a pure  $\alpha$ -Fe<sub>2</sub>O<sub>3</sub> phase (JCPDS 33-0664). (d) Low magnification TEM image showing the angle between the corresponding anisotropic growth directions.....P.38

**Figure 2.12** Low magnification FE-SEM images of  $\alpha$ -Fe<sub>2</sub>O<sub>3</sub> fractal structures synthesized with a K<sub>3</sub>[Fe(CN)<sub>6</sub>] concentration of (C,A) 3.8 mM and (D,B) 38 mM at 180°C for 8 and 20 h (bottom and top), respectively.....P.39

**Figure 2.13** High magnification SEM images of branched  $\alpha$ -Fe<sub>2</sub>O<sub>3</sub> structures synthesized with a K<sub>3</sub>[Fe(CN)<sub>6</sub>] concentration of 3.8 mM at 180°C for (A) 1.5, (B) 2.0, (C) 3.0, (D) 4.0 and (E) 8.0 h. (F) Average crystalline (grain) size “D” graph showing a typical crystal growth pattern with several dissolution-recrystallization cycles through the aging time. ....P.41

**Figure 2.14** Time-dependent pXRD patterns, showing the crystal growth (aging) process (from red to purple), of the typical branched  $\alpha$ -Fe<sub>2</sub>O<sub>3</sub> fractal structures synthesized with a K<sub>3</sub>[Fe(CN)<sub>6</sub>] concentration of 3.8 mM at 180°C from 2 to 48 h.....P.42

**Figure 2.15** Low magnification FE-SEM images of branched  $\alpha$ -Fe<sub>2</sub>O<sub>3</sub> fractal structures synthesized with a K<sub>3</sub>[Fe(CN)<sub>6</sub>] concentration of 4 mM at 180°C for 20 h in bi-solvent H<sub>2</sub>O-to-EtOH volume ratios of (A) 3 : 1, (B) 1 : 1 and (C) 1 : 3. (D) pXRD pattern of the corresponding products synthesized under a variable mixture in H<sub>2</sub>O:EtOH ratios, which are outlined as 3 : 1 (blue), 1 : 1 (red) and 1 : 3 (black), respectively.....P.44

**Figure 2.16** Low magnification FE-SEM images of branched  $\alpha$ -Fe<sub>2</sub>O<sub>3</sub> fractal structures synthesized with a K<sub>3</sub>[Fe(CN)<sub>6</sub>] concentration of 4 mM at 180°C for 20 h in bi-solvent H<sub>2</sub>O-to-DMF volume ratios of (A) 1 : 0, (B) 3 : 1, (C) 1 : 1 and (D) 1 : 3. (E-G) Size distribution data and (H) pXRD pattern of the corresponding products synthesized under a variable mixture in H<sub>2</sub>O:DMF ratios, which are outlined as (E) 3 : 1 (blue), (F) 1 : 1 (red) and (G) 1 : 3 (black), respectively.....P.45

**Figure 2.17** UV-visible spectra of the (A) as synthesized branched  $\alpha$ -Fe<sub>2</sub>O<sub>3</sub> fractal structures, namely secB3D (black), tertD2D (red), tertD3D (blue), secS2D (green) and hypB2D (purple), dispersed at the concentration of 0.1 g/L in H<sub>2</sub>O (with an exception of tertD3D at 25 mg/L), and (B) azo-type textile dyes, namely AR (orange), CR (red), CB (black), DB (blue) and MO (yellow) dissolved at a concentration of 20  $\mu$ M in H<sub>2</sub>O.....P.47

**Figure 2.18** UV-visible spectral changes of (A) CB, (B) DB and (C) MO as a function of irradiation time with H<sub>2</sub>O<sub>2</sub>, as the additive, in the presence of secS2D and secB3D (depicted in A and B, C). Photo-Fenton oxidation of (D) CB, (E) DB, and (F) MO upon exposure to all five distinctive  $\alpha$ -Fe<sub>2</sub>O<sub>3</sub> fractal structures under periodic visible (white) light illumination in the presence of H<sub>2</sub>O<sub>2</sub>.....P.50

**Figure 2.19** Photo-Fenton degradation efficiency (%), as calculated by  $(1 - C/C_0) \times 100$ , of (A) CB, (B) DB and (C) MO as a function of irradiation time with H<sub>2</sub>O<sub>2</sub>, as the additive, in the presence of blank (black), secB3D (red), tertD2D (blue), tertD3D (green), secS2D (purple) and hypB2D (orange). Pseudo-first order kinetics of photo-Fenton oxidation of (D) CB, (E) DB, and (F) MO upon exposure to all five distinctive  $\alpha$ -Fe<sub>2</sub>O<sub>3</sub> fractal structures under periodic visible (white) light illumination in the presence of H<sub>2</sub>O<sub>2</sub>.....P.52

**Table 2.1** Pseudo-first order rate constants of photo-Fenton oxidation of CB, DB, and MO upon exposure to all five distinctive  $\alpha$ -Fe<sub>2</sub>O<sub>3</sub> fractal structures under periodic visible (white) light illumination in the presence of H<sub>2</sub>O<sub>2</sub>.....P.53

# Chapter 1: Introduction

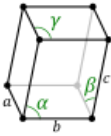
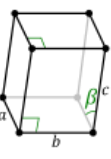
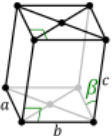
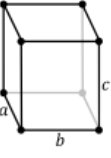
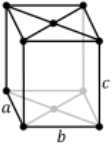
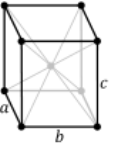
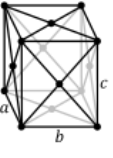
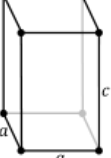
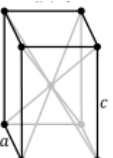
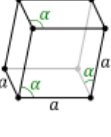
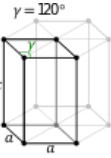
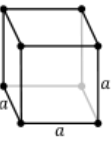
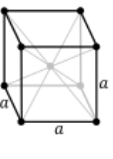
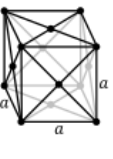
## 1.1 Background of Crystal Structure

### 1.1.1 Basic Concepts of Crystal Structure

Fundamental constituents of inorganic nanostructures commonly rely on the concept of the unit cell. In crystallographic terms, the fundamental “building block” define itself as the smallest repeating unit via the translational vectors  $(\vec{a}, \vec{b}, \vec{c})$  along the corresponding axial length constants of  $a$ ,  $b$ , and  $c$ . Certainly, within the unit cell, the atomic groupings, called the *motif*, defined around lattice points in space should be congruent to adjacent cells by translational symmetry, thereby constituting the so-called “basis set” of the crystal lattice. In summary, all crystal structures are periodic arrangements of atoms in space, which are defined by the lattice (or unit cell) and the basis set.

In 1848, Auguste Bravais demonstrated that there are only fourteen possible space lattices, as periodically arranged points in space, with distinct geometry and symmetry.<sup>1</sup> These mathematically proven lattice types are now called “Bravais lattices”. The lattices were subsequently categorized into seven different crystal systems, each with its own geometric restrictions except for the triclinic system.<sup>2</sup> As summarized in Table 1.1, both the rhombohedral and hexagonal crystal system belong to the trigonal crystal family though they differ by symmetry. In the total synthesis of inorganic nanostructures, crystal structures are typically determined by the chemical transformation of specific crystalline phases, which eventually direct the overall morphology of synthetic crystals, examinable in the microscale.<sup>3</sup>

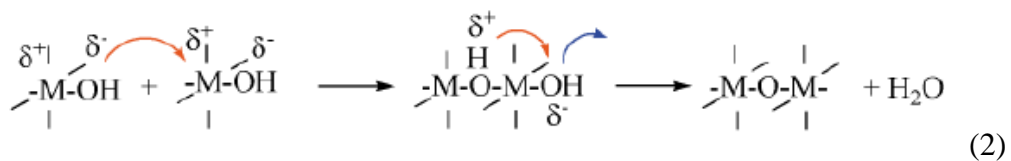
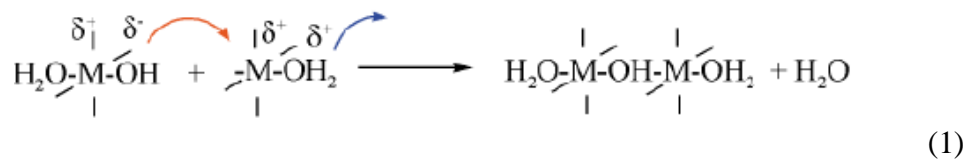
**Table 1.1** Summary and categorization of the Bravais lattices to the respective point groups, crystal systems and families.

Six Crystal Families	Seven Crystal Systems	Point group	14 Bravais Lattices			
			Primitive	Base- Centered	Body- Centered	Face- Centered
Triclinic		$C_i$				
Monoclinic ( $\alpha = \gamma = 90^\circ$ )		$C_{2h}$				
Orthorhombic ( $\alpha = \beta = \gamma = 90^\circ$ )		$D_{2h}$				
Tetragonal ( $a = b$ ) ( $\alpha = \beta = \gamma = 90^\circ$ )		$D_{4h}$				
Trigonal	Rhombohedral ( $a = b = c$ ) ( $\beta = \gamma = 90^\circ$ )	$D_{3d}$				
	Hexagonal ( $a = b$ ) ( $\alpha = \beta = 90^\circ$ ; $\gamma = 120^\circ$ )	$D_{6h}$				
Cubic ( $a = b = c$ ) ( $\alpha = \beta = \gamma = 90^\circ$ )		$O_h$				

### 1.1.2 From “Clusters-to-Lattice”

Iron is indeed one of the most abundant elements on Earth.<sup>4</sup> Its widespread nature reveals itself in nearly all aspects of the global system: the atmosphere, lithosphere, hydrosphere, and the biosphere. For industrial use, iron is found in minerals and ores consisting mainly of magnetite (Fe<sub>3</sub>O<sub>4</sub>), hematite (α-Fe<sub>2</sub>O<sub>3</sub>) and goethite (α-FeOOH).<sup>5,6</sup> As distinguished by the differing phases of the α-polymorphs, as mentioned above, α-Fe<sub>2</sub>O<sub>3</sub> and FeOOH belong to the iron oxide and iron(oxy-, hydro-)xide family, respectively.

The widely accepted underlying mechanisms in the formation of the crystalline lattice are a) hydrolysis and b) condensation, which are commonly known in sol-gel processes.<sup>7,8</sup> Hydrolysis is the thermodynamically favourable mechanism as it is inherently exothermic, which results in the hydroxylated form of the original molecular precursor as the monomer. Subsequently, two of the same hydroxylated monomers within proximity undergo condensation to form a molecular dimer, which further assembles into a lattice.<sup>9</sup> Condensation is mainly achieved by the mechanisms: (1) olation and (2) oxolation, as shown respectively in the following:



Olation takes place in a single elementary step to form the hydroxo-bridge, whereas oxolation occurs in a “two-step” associative mechanism to form an oxo-bridge. Note that both mechanisms release H<sub>2</sub>O as the byproduct, thus the categorization of both olation and oxolation as condensation mechanisms. A pre-nucleation cluster was hypothesized to form when two dimers of [Fe(OH)<sub>2</sub>(OH<sub>2</sub>)]<sup>2+</sup> chelate via a hydroxo-bridge into a tetrameric unit of [Fe<sub>4</sub>(OH)<sub>4</sub>(OH<sub>2</sub>)<sub>12</sub>]<sup>4+</sup> (Figure 1.1).<sup>9</sup> As represented, it was speculated that the molecular clusters form an intermediate structure, such as the Fe(OH)<sub>2</sub>.

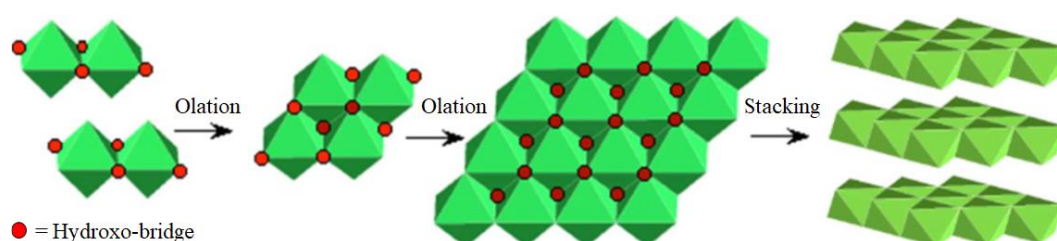


**Figure 1.1** Schematic representation of the formation process of ferrous hydroxide, termed Fe(OH)<sub>2</sub>, isostructural to brucite.<sup>9</sup>

### 1.1.3 From “Phase to Morphology”

Phase control, undoubtedly, is one of the pillars of inorganic colloidal synthesis. Phase control often involves the transition between polymorphs, such as the well-established oxidation of β-FeOOH to α-Fe<sub>2</sub>O<sub>3</sub>.<sup>10,11</sup> Since different mineral phases differ in symmetry and composition of the unit cell, a phase transition in the condensed matter phase is a dynamic process, which often requires an external stimulus, such as by applying temperature, pressure...etc., or a combination of external factors.

Akaganeite (β-FeOOH), an intermediate crystalline phase to the thermodynamically stable hematite (α-Fe<sub>2</sub>O<sub>3</sub>), belongs to the iron(oxy-,hydr-)oxide

family of iron oxides.<sup>5,6</sup> In crystallography, its crystal system possesses a monoclinic symmetry with the space group of  $I2/m$ . In Bravais lattices, its unit cell is distinguishable by its anion lattice of body centered cubic (*bcc*) packing of anions. To induce  $\beta$ -FeOOH formation, a high concentration of chloride anions,  $[\text{Cl}^-] > 10$  mM in the addition of  $\text{FeCl}_3$ , is sufficient in the hydrolysis step as shown in Figure 1.2.<sup>12</sup> As depicted, the crystal structure has arranged dimers of  $(\text{FeO}_6)^{6-}$  projected along the *b*-axis, forming an open channel to stabilize the chloride anion. However, with the precursor of  $\text{FeCl}_3$ , the transition would occur via the formation of a six-line ferrihydrite intermediate. The ferrihydrite is presumed to be elusive as the nucleation kinetics of  $\beta$ -FeOOH is an immediate process ( $\tau \sim 10^{-3}$ s), thus only a few detailed studies have been reported on six-line ferrihydrite.<sup>13</sup>

Goethite ( $\alpha$ -FeOOH), as the abbreviation implies, also belongs to the iron(oxy-,hydr-)oxide family of iron oxides. Thus, it is also an intermediate phase to the thermodynamically stable hematite ( $\alpha$ - $\text{Fe}_2\text{O}_3$ ). Its crystal system possesses orthorhombic symmetry with the space group of *pnma*. As for the lattice type, its unit cell is composed of the hexagonal close packing (*hcp*) of anions, sharing resemblance to hematite ( $\alpha$ - $\text{Fe}_2\text{O}_3$ ). Experimentally, if an initial concentration of  $[\text{Cl}^-] = 10$  mM were to be used,  $\alpha$ -FeOOH would not be expected to form as the transformation favours  $\beta$ -FeOOH to  $\alpha$ - $\text{Fe}_2\text{O}_3$  as shown in Figure 1.2. However, a recent study suggests that it is possible to induce  $\alpha$ -FeOOH formation via the akageneite-goethite-hematite pathway if silicates with enough hydroxyl groups were added as the template for nucleation.<sup>14</sup> As a reasonable hypothesis, the stabilized channels with chloride as the core in  $\beta$ -FeOOH is subject to anion exchange with hydroxide anions, resulting in the structural rearrangement into  $\alpha$ -

FeOOH. This is further re-enforced by prior experiments in which potassium hydroxide was added as the precipitating agent to increase the pH.<sup>15</sup> Indeed, experiments reveal that mostly  $\alpha$ -FeOOH has been formed at lower temperatures after aging as the two-line ferrihydrite was obtained via immediate precipitation.

Hematite ( $\alpha$ -Fe<sub>2</sub>O<sub>3</sub>) is the most thermodynamically stable phase, which is the end product of most iron (oxy-,hydro-)xides and iron oxides. Its *hcp* unit cell packing is oriented with the trigonal crystal symmetry, which its motif is spanned within the space group of *R-3c*. For most polymorphs at higher temperatures (> 120 °C), the transition via oxidation to  $\alpha$ -Fe<sub>2</sub>O<sub>3</sub> is inevitable at the presence of O<sub>2</sub>.<sup>6</sup> Notably,  $\alpha$ -Fe<sub>2</sub>O<sub>3</sub> undergoes the dissolution-recrystallization mechanism at high temperatures via the hydrothermal method.<sup>16</sup> Arguably, the growth of hematite crystals likely occurs via the phase transformation on the surfaces of the respective  $\alpha$ -/ $\beta$ -FeOOH template, which in turn depends on the synthetic conditions (e.g. pH value).<sup>15</sup> Furthermore, at a low iron precursor concentration, [Fe<sup>3+</sup>] < 20 mM from FeCl<sub>3</sub>, the colloidal suspension of crystals would directly transform into  $\alpha$ -Fe<sub>2</sub>O<sub>3</sub> which likely occurs without templated phase transitions.

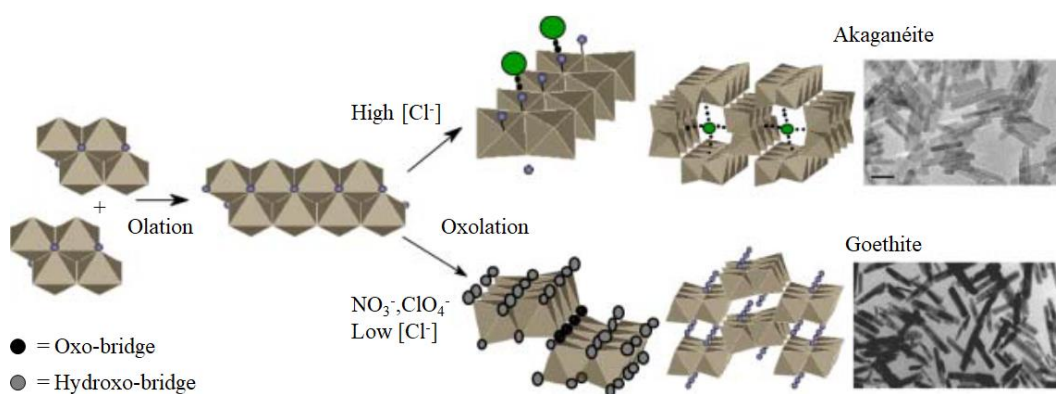


**Figure 1.2** Transformation pathways of akaganeite ( $\beta$ -FeOOH) and goethite ( $\alpha$ -FeOOH) via dissolution-recrystallization of thermodynamic unstable ferrihydrite.<sup>9</sup>

#### **1.1.4 Introduction to Nucleation and Growth**

To facilitate our discussion, we had to first introduce some terminology to describe the mechanisms of colloidal synthesis. Briefly, a classical crystal growth process consists of nucleation and growth stages,<sup>35</sup> which are respectively affected by the intrinsic crystal structure and external (experimental) conditions. Nucleation processes generally may be divided into primary and secondary nucleation. Primary nucleation is the case of nucleation without the presence of other crystalline matter as defined by Mullin.<sup>39</sup> Secondary nucleation, on the other hand, refers to nucleation in the presence of other physical forces (e.g. fluid shear, collisions between pre-existing crystalline nuclei,...etc.). Crystal growth is traditionally defined by Ostwald ripening, coined after Wilhelm Ostwald (1896), as the growth of larger particles at the expense of smaller ones, mainly due to their increased relative surface energies. In the case of dendritic hematite ( $\alpha$ -Fe<sub>2</sub>O<sub>3</sub>), a reversed mechanism of crystal growth was proposed to have taken place.<sup>40</sup> Furthermore, the dissolution-recrystallization mechanism shows the morphological evolution of these structures (as discussed in our study). Interested readers should explore this topic highlighted elsewhere.<sup>35</sup>

## **1.2 Morphological Control of Crystals**

### **1.2.1 Inherent Anisotropic Growth**

All crystals are inherently anisotropic, meaning that the growth of crystals depend on the relative growth rates of different crystalline planes. As an example,  $\beta$ -FeOOH is often characterized by its acicular shape in Figure 1.2 due to its anisotropic growth along the [001] direction.<sup>6</sup> The main cause for its

spindle shape originates from the faster growth rate along a specific direction. By exploiting this property, high aspect ratios of hematite nanorods were synthesized via the 1,2-propanediamine-assisted hydrothermal method.<sup>33</sup> It is noteworthy that inorganic solid-state surfaces with higher index planes usually possess enhanced growth rates. In the synthesis of branched hematite ( $\alpha$ -Fe<sub>2</sub>O<sub>3</sub>) structures from K<sub>3</sub>[Fe(CN)<sub>6</sub>], it was previously reported that the structures demonstrate fast anisotropic growth along [10-10].<sup>17</sup> It was speculated that the branched growth pattern resulted from a diffusion-limited mechanism due to the weak dissociation tendency of the [Fe(CN)<sub>6</sub>]<sup>3-</sup> ions ( $K_s = 1.0 \times 10^{42}$ ).

### 1.2.2 Multipod & Polyhedral Structures

The morphological control of nanostructures relies on the relative growth rates of crystalline planes. Multipod structures are often the result of kinetic control; whereas polyhedral structures result from thermodynamic control in synthetic systems. Few literature studies have discussed these relationships between the transformation of multipod and polyhedral structures, especially in the area of iron oxides.<sup>18</sup> As for multipod structures of magnetite (Fe<sub>3</sub>O<sub>4</sub>), only tetra-, hexa-, and octopods have been reported thus far.<sup>19-21</sup> Unlike polyhedral structures,  $\alpha$ -Fe<sub>2</sub>O<sub>3</sub> multipods are less prevalent as only the two-dimensional “snowflake-like” fractal structures were reported.<sup>22</sup> Unlike Fe<sub>3</sub>O<sub>4</sub>,  $\alpha$ -Fe<sub>2</sub>O<sub>3</sub> polyhedrons, which some are shown in Figure 1.3(a) and (b), diversify as colloidal cubic,<sup>23,24</sup> rhombohedral,<sup>25</sup> octahedral,<sup>26</sup> hexagonal bipyramidal,<sup>27-29</sup> tetrahedral bipyramidal,<sup>30</sup> dodecahedral, and octadecahedral-shaped structures have been reported.<sup>31-32</sup>

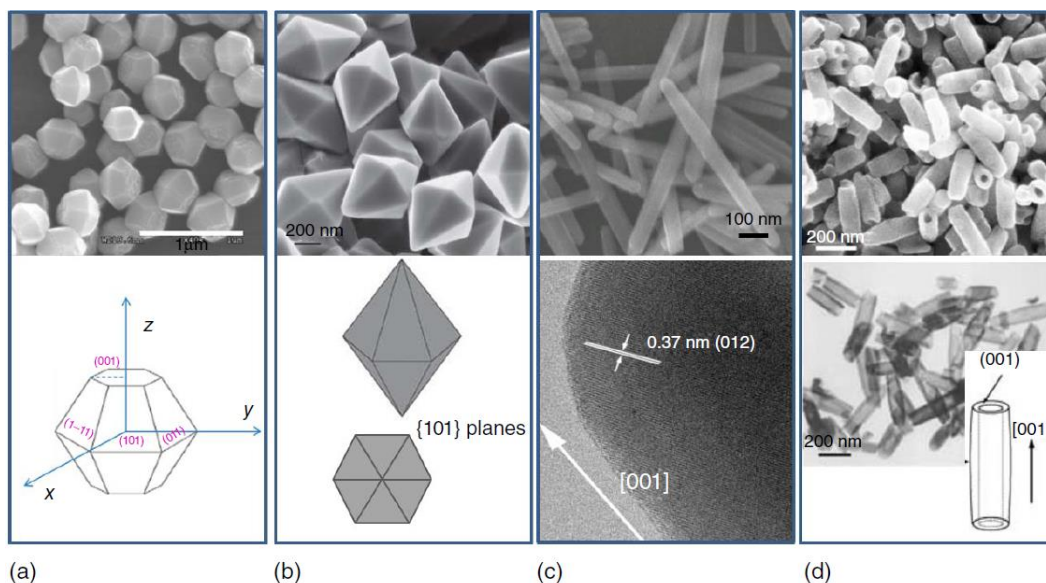


**Figure 1.3** Images of single-crystalline hematite morphology obtained using different capping agents, namely (a) truncated hexagonal bipyramidal synthesized using carboxymethyl cellulose and hydrazine,<sup>29</sup> (b) dodecahedral as hexagonal bipyramidal shape synthesized with the aid of F<sup>-</sup> anion,<sup>31</sup> (c) nanorods with high aspect ratios synthesized by 1,2-propanediamine-assisted hydrothermal method,<sup>33</sup> and (d) hollow nanotubes fabricated by one-step hydrothermal method in an aqueous  $\text{NH}_4\text{H}_2\text{PO}_4$  solution.<sup>34</sup>

### 1.2.3 Dissolution-Recrystallization Mechanism

Dissolution and recrystallization are common among all crystalline materials under aging conditions. The relative dissolution and recrystallization rates strongly depend on the surface energy of the colloidal particles formed. Since the Ostwald ripening process is also dependent on the relative surface energy among different sized particles, this context is sometimes discussed in a similar context to the dissolution-recrystallization pathway.<sup>35</sup> An example of this pathway to form unique colloidal structures include the one-step hydrothermal method of  $\text{FeCl}_3$  dissolved in aqueous  $\text{NH}_4\text{H}_2\text{PO}_4$  solution, in which the sides were first protected by the use of  $\text{Na}_2\text{SO}_4$  for the selective reductive dissolution.<sup>34</sup>

## 1.3 Wet Chemical Synthetic Methods

### 1.3.1 Micro-Emulsion Synthetic Method

Micro-emulsion often revolves around the use of surfactants as soft templates as part of the synthesis. Commonly, mesoporous silica nanoparticles (MSNs) are synthesized by this method.<sup>54</sup> Typically, a surfactant of choice, such as hexadecyltrimethylammonium bromide (CTAB) and sodium dodecyl sulphate (SDS), would have to dissolve in aqueous solution above the critical micellar concentration (CMC) to form micelles as micro-reactors.<sup>36</sup> Once the micelles have stabilized and self-assembled, silica precursors were deposited into the soft templates for hydrolysis and condensation to form the mesoporous nanoparticles. The templates would further be removed to obtain the final purified products. In a prior study,<sup>48</sup> interestingly, 5 mM of CTAB was added into the hydrothermal synthesis with 10 mM of the  $K_3[Fe(CN)_6]$  maintained at 180°C for 12 h to yield the single-layered “snowflake-like” fractal structures.

### 1.3.2 Seeded Growth Synthetic Method

Seeded growth, sometimes termed as “homogeneous seeded-growth”, generally rely on solid-phase templates, called the crystalline nuclei. In the formation of goethite ( $\alpha$ -FeOOH), seeded growth approaches are typically mediated via an intermediate template of two-line ferrihydrites.<sup>15</sup> However, it should be noted that the terminology of “seeds” is often poorly defined in length specification. In geochemical studies, this phenomenon has been widely explored especially in the formation of metal oxides,<sup>15-16</sup> appealing to geologists and chemists alike. To this date, there are no studies that successfully demonstrate the hierarchical assembly of dendritic hematite ( $\alpha$ -Fe<sub>2</sub>O<sub>3</sub>) structures via this synthetic approach.

### 1.3.3 Substrate-Based Epitaxial Growth

Substrate-based epitaxial growth, sometimes termed as “heterogeneous seeded-growth”, also rely on solid-phase templates, commonly on the surface of thin films. Recently, thermal decomposition of  $\text{Fe}(\text{CO})_5$  on hexagonal nanoplatelets of  $\alpha\text{-Fe}_2\text{O}_3$  demonstrated an enhancement in magnetic resonance imaging.<sup>37</sup> Classical examples of epitaxial growth are represented by perfect lattice matching of  $\text{SnO}_2$  to the *hcp* anion packing of  $\alpha\text{-Fe}_2\text{O}_3$  as depicted in Figure 1.4.<sup>38</sup> Nanostructures, such as nanoflowers, are believed to be formed as a result of poor lattice matching of the depositing inorganic precursors to the substrate. Interested readers should explore the studies of epitaxial growth on  $\alpha\text{-Fe}_2\text{O}_3$ .<sup>38</sup>

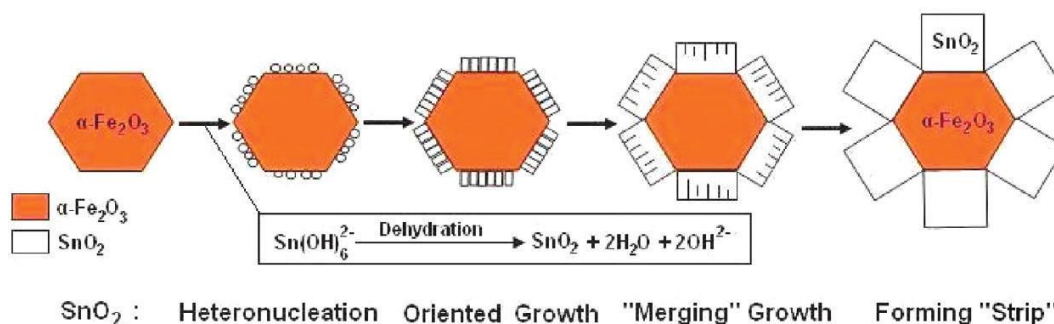


**Figure 1.4** Schematic representation showing the “step-by-step” mechanisms of epitaxial growth in the example of  $\text{SnO}_2$  nanorods growing on  $\alpha\text{-Fe}_2\text{O}_3$  substrates.<sup>38</sup>

## 1.4 Chemistry of Fenton Oxidation

Classical Fenton oxidation is well known in its ability to facilitate oxidation by using  $\text{Fe}^{2+}$ , which usually relies on hydrogen peroxide ( $\text{H}_2\text{O}_2$ ) as the oxidant.<sup>41</sup> The outcome of Fenton oxidation, sometimes termed as “mineralization”, often oxidizes unwanted complex organic constituents into the desirable thermodynamic products of  $\text{CO}_2$  and  $\text{H}_2\text{O}$ . Although traditional Fenton systems are relatively quick (in reaction rates) and reliable, due to its simplicity in optimization and control, there are some intrinsic drawbacks that limits its widespread use, specifically in the area

of environmental remediation. This is the case especially due to its limiting pH range (optimal pH  $\sim 3 - 4$ ),<sup>42,43</sup> and the accumulation of ferric oxide sludge, which further decreases the oxidation rate in the long-run. While there are some simpler methods to resolve these issues, such as by adding hydroxylamine ( $\text{NH}_2\text{-OH}$ ),<sup>43</sup> others have sought out more environmentally friendly alternatives. One such alternative is by employing heterogeneous Fenton oxidation, which eases the applicational cost due to its inherent recyclability.<sup>44,45</sup> Both approaches expand the operational pH range. Obviously, Fenton oxidations mediated in the dark, so called “dark Fenton”, has a clear advantage due to its reduced operational cost. Unfortunately, Fenton oxidation under illumination, as known as “photo-Fenton” is necessary for some heterogeneous catalysts.<sup>41</sup> To highlight photocatalysis, photo-induced charge transfer of electrons, as induced by visible light, is necessary for the electron-hole separation as part of the redox cycle. Ideally, the electron as supplied by photo-absorption, mediates the reduction of  $\text{Fe}^{3+}$ , usually through an electron mediator (e.g. a colorimetric dye) via the “dye-sensitization” mechanism.<sup>46</sup> In the Haber-Weiss mechanism (1934), we are mainly concerned with hydroxyl radicals ( $\cdot\text{OH}$ ), as a dominant species from the splitting of  $\text{H}_2\text{O}_2$  (as reported elsewhere),<sup>47</sup> which are highly reactive (with a half-life of  $10^{-5}$  s) and non-selective in their attack of organic pollutants. Presuming the dye-sensitized mechanism, in our experimental design, we supplied an excess amount of  $\text{H}_2\text{O}_2$  for the splitting to generate reactive  $\cdot\text{OH}$  for the degradation of the azo-type dye, as our model pollutant, under white light illumination. Prior studies mentioned that the exposed planes of predominantly {10-10} facets provide higher photocatalytic activity.<sup>40</sup> We have poised to explore the “structure-to-activity” relationships of our as-synthesized inorganic colloidal particles within the area of photo-catalytic heterogeneous

Fenton oxidation.

## 1.5 Expected Findings of Study

A great deal of effort was spent on discovering novel higher ordered structures of  $\alpha\text{-Fe}_2\text{O}_3$  as only the “snowflake-like” fractal structures, with six equivalent crystallographic directions, were ever discovered as of date.<sup>22</sup> We expected that, with proper tuning of synthetic parameters, novel structures of  $\alpha\text{-Fe}_2\text{O}_3$  may be generated as a result of morphological control. Therefore, providing means to test for the “structure-to-activity” relationship of novel inorganic structures.

## 1.6 Outline of the Thesis

The formation of the  $\alpha\text{-Fe}_2\text{O}_3$  crystals was thoroughly studied in hopes of discovering novel structures for model studies, such as the use of inorganic structures in photocatalytic degradation experiments. We have noted in prior to this synthetic work that hematite ( $\alpha\text{-Fe}_2\text{O}_3$ ), the most thermodynamically stable phase of iron oxides, belongs to the structurally complex trigonal family.

As mentioned, the main work of this thesis is entirely focused on the “facile synthesis and fine morphological tuning of branched hematite ( $\alpha\text{-Fe}_2\text{O}_3$ ) crystals for photodegradation of azo-type dyes”. Firstly, we start by an introduction explaining the motivation behind our work. Secondly, we outline the synthetic scheme of hexacyanoferrate-derived branched  $\alpha\text{-Fe}_2\text{O}_3$  microcrystals for the purpose of directing our discussion. The detailed experimental procedure is arranged at the end of the thesis chapter for your reference. Thirdly, our discussion would be compiled with the results to ease the reviewing process.

For more information, our results and discussion are arranged for your convenience in the following manner: (1) surface morphology analysis from field-emission scanning electron micrograph (FE-SEM), (2) structural and vibrational information analysis, (3) growth mechanism of typical dendritic hematite ( $\alpha$ -Fe<sub>2</sub>O<sub>3</sub>), (4) the effect of EtOH- and DMF-to-H<sub>2</sub>O volume ratios and (5) photo-Fenton oxidation of azo-type textile dyes.

## **Chapter 2: Facile Synthesis & Fine Morphological Tuning of Branched Hematite ( $\alpha$ -Fe<sub>2</sub>O<sub>3</sub>) Crystals for Photodegradation of Azo-Type Dyes**

### **2.1 Introduction**

Branched structures, commonly spherulites and dendrimers,<sup>60-62</sup> have found their use in numerous areas of application such as in catalysis, drug delivery, optical and electrochemical devices. Conventionally, these materials are applied because of their high pore volumes and large surface areas. Multi-generations of these hierarchical materials dramatically differ in the physicochemical properties.<sup>54</sup> Dongyuan Zhao et al. previously devised the hierarchical synthesis of dendritic mesoporous silica nanoparticles (MSNs), and compared them via the differed release profiles by using bovine  $\beta$ -lactoglobulin as the model protein. Such dendritic materials with tunable properties are of interest due to its potential in drug delivery applications. To this date, few studies have reported such well-defined hierarchical inorganic mesoporous nanostructures. Nanoflowers, on the other hand, are fibrous materials which are not as structurally defined but possess high surface areas. Commonly, nanoflowers may serve as heterogeneous supports for catalytic applications.<sup>63</sup>

In our work, we wish to study the synthetic parameters of the branched  $\alpha$ -Fe<sub>2</sub>O<sub>3</sub> structures in detail. We hope that, by (1) understanding the synthesis, novel structures could be synthesized by modulating the relative growth rates of the branched fractal structures. To demonstrate the viability of our approach, we further (2) apply our knowledge to the bi-solvent hydrothermal environment to rationally design the branched colloidal crystals.

## 2.2 Results & Discussion

**Formation of Dendritic  $\alpha$ -Fe<sub>2</sub>O<sub>3</sub> Fractal Structures.** Synthesis of branched, also known as dendritic, hematite ( $\alpha$ -Fe<sub>2</sub>O<sub>3</sub>) structures were optimized based on the concepts of pre-nucleation, facet-directed growth,<sup>17,22</sup> acidity/basicity, solvent's boiling point, polarity and viscosity. All synthetic variants of the branched  $\alpha$ -Fe<sub>2</sub>O<sub>3</sub>, as synthesized via the hydro-/solvothermal reaction of 4 mM K<sub>3</sub>[Fe(CN)<sub>6</sub>] at 180°C for 20 h, were summarized (Fig. 2.1). On the basis of morphological control, the hierarchical self-assembly of branched  $\alpha$ -Fe<sub>2</sub>O<sub>3</sub> is widely regarded to occur under non-equilibrium conditions due to the weak dissociation constant of [Fe(CN)<sub>6</sub>]<sup>3-</sup> ions ( $K_{\text{eq}} = 1.0 \times 10^{42}$ ).<sup>17</sup> On the other hand, the high stability of [Fe(CN)<sub>6</sub>]<sup>3-</sup> ions ensures that the concentration of free Fe<sup>3+</sup> remains low during the course of hydrothermal synthesis. Thus, such synthetic approach tends to be “calcination-free”, meaning free of any need for phase transformation into the thermodynamic polymorph. In principle, a classical crystal growth process consists of nucleation and growth stages,<sup>35</sup> which are respectively affected by the intrinsic crystal structure and external conditions. By considering the “diffusion-limited aggregation” (DLA) pathway,<sup>55</sup> we expected the growth to proceed via the oriented aggregation of primary particulate clusters, presumably a combination of nucleated amorphous and crystalline seeds.<sup>56</sup> Earlier studies have hypothesized that “oriented aggregation” is preceded by localized random orientation of primary particles via Brownian motion until the satisfaction of favourable crystallographic order, allowing the irreversible particle-to-particle attachment via lattice matching.

With respect to the anisotropic nature of facet growth, the dendritic morphologies of  $\alpha$ -Fe<sub>2</sub>O<sub>3</sub> were categorized based on the structural properties of the

1) degree of branching and 2) overall orientation of the particles relative to the horizontal plane of the underlying substrate. Divergence from the primary 1<sup>o</sup> growth direction, defined here as the primary 1<sup>o</sup> “*stem*”, would justify as secondary 2<sup>o</sup> branching. Thus, further differentiation from the secondary 2<sup>o</sup> growth, defined as the “*branch*”, would justify as tertiary 3<sup>o</sup> branching of “*leaflet*” and so on. To demonstrate the viability of our approach, all the branched particles were examined morphologically (Fig. 2.2). At the microscopic scale, we ascribe the corresponding particles as synthesized into 2<sup>nd</sup> generation three-dimensional (*secB3D*), 3<sup>rd</sup> generation two-dimensional (*tertD2D*), 3<sup>rd</sup> generation three-dimensional (*tertD3D*), “*starfish-like*” two-dimensional (*secS2D*) and hyper-branched two-dimensional (*hypB2D*) micro-dendrites, respectively.

**Surface Morphology Analysis from FE-SEM.** For the 2<sup>nd</sup> generation three-dimensional micro-dendrites (*secB3Ds*), the average 1<sup>o</sup> “*stem*” and 2<sup>o</sup> “*branch*” lengths are 4.6147 and 1.3263  $\mu\text{m}$ , respectively (Fig. 2.3 A). The dispersity of inorganic colloidal particles is defined by the coefficient of variation (*CV*), which is calculated by the standard deviation (*S.D.*) divided by the mean ( $\mu$ ), resulting in 0.3086 and 0.3967, correspondingly. Although the surface morphologies seem relatively uniform (Fig. 2.2 A and F), the variations in size distribution of 1<sup>o</sup> and 2<sup>o</sup> lengths suggest that the branched *secB3D* particles are not considered to be mono-dispersed. Similarly, the average 1<sup>o</sup> branching angle, between the 1<sup>o</sup> *stem* and 2<sup>o</sup> *branch* lengths, was determined to be 62.1949 with a *CV* of 0.0810. Despite the variability of branching angle being significantly less (Fig. 2.3 F), the calculated value did not reach the ideal *CV* of 0.01 as suggested by Schweiger.<sup>49</sup> In other words, this degree of variation, which may be used to compare between different samples

of branched  $\alpha$ -Fe<sub>2</sub>O<sub>3</sub>, should ideally be varying at only 1% to be considered as a “mono-dispersed” batch of colloidal particles. Moreover, inorganic colloids with dendritic morphologies are known to form via diffusion-limited aggregation (DLA), widely regarded as the “DLA model”.<sup>55</sup> Thereby, any variation in the overall particle size, resulting from the 1° *stem* and 2° *branch* lengths, may just be a consequence in the variability of nuclei size at the early stages of heterogeneous nucleation, due to the “mesh-like” nature of the metal precursor used. On the contrary, any variation in the branching angle may implicate the effects of micro-strain in the crystalline lattice, which indirectly supports the hypothesis of oriented aggregation as the thermodynamic pathway to form the resulting particles.

The incorporation of ethanol (EtOH) for the hydrolysis and condensation of inorganic colloidal crystals has been demonstrated as a viable and successful synthetic strategy in morphological control.<sup>28</sup> Besides modulating the basicity of the aqueous medium, its use is justified by the lower boiling point (78.37°C) of EtOH. However, the main synthetic variable is likely the change in solubility of the K<sub>3</sub>[Fe(CN)<sub>6</sub>] precursor via the addition of EtOH. As such, morphological change in the selective growth of *secB3D* may be mediated as rapid primary facet growth facilitates along the [1-100] direction.<sup>17</sup> The single morphological structure (Fig. 2.2 K) also reveals that only secondary 2° branching from the primary 1° “stem” was possible due to that specific anisotropic growth direction. The topology of the *secB3D*’s surface reveals that the particle of interest does not completely reside along the horizontal plane of the sample holder. In fact, the brighter regions (on the *right* side) represent the edges while dark regions (on the *left* side) represent the recesses, which are lying parallel along the horizontal surface of the substrate. As a

result, we confirmed that the as synthesized *secB3D*s are three-dimensional in nature. Due to the rod-like (or spindle) characteristic of each branch, we further determined that the structural thickness to be around 229 nm, as consistent to a prior study.<sup>50</sup> It has been previously suggested that the “branch” or so-called “sub-branch” with a rod-like shape is the fundamental building block of the entire dendritic or fractal structure. To justify the origin of enhanced anisotropic growth along the specific [1-100] direction, “spatial confinement” was proposed for which subsequent growth could only occur diagonally, according to the crystal structure, alongside the two crystallographically equivalent directions, [10-10] and [0-110], leading to the symmetric 2<sup>o</sup> branches aligned in parallel on each side.<sup>22</sup> As a result, almost all of our as synthesized products (Fig. 2.1) resemble “leaf-like” structures in the morphological context.

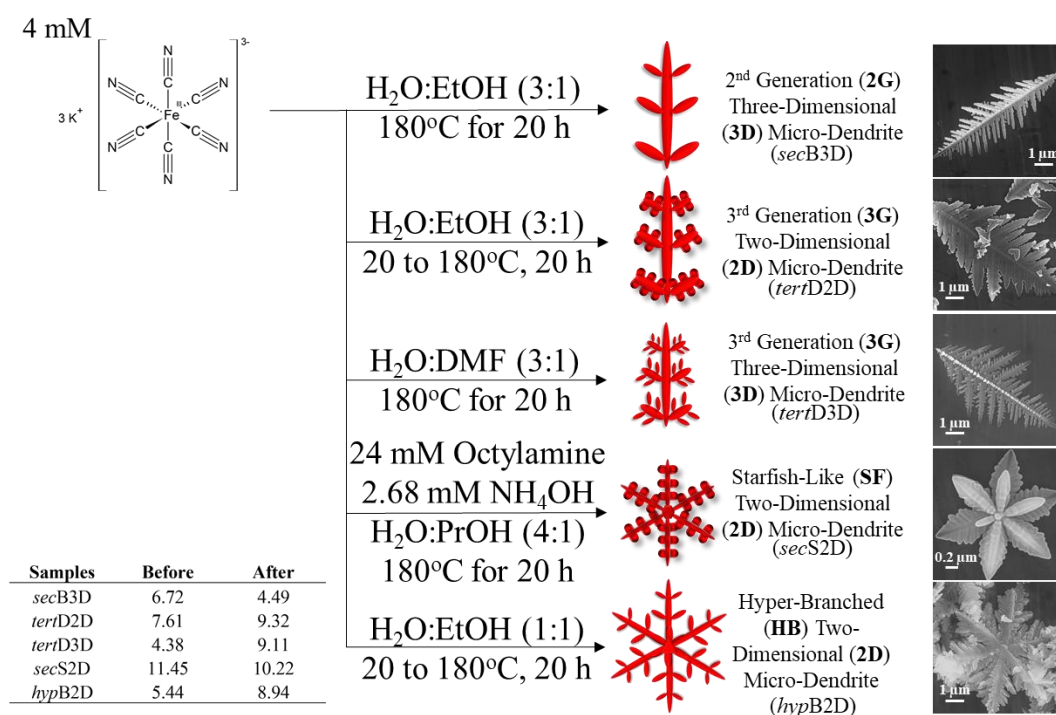


**Figure 2.1** Synthetic scheme of various dendritic-shaped  $\alpha$ - $\text{Fe}_2\text{O}_3$  fractal structures via a solvothermal reaction in bi-solvent medium. *Insert*: Table of the supernatant pH before and after the solvothermal synthesis.

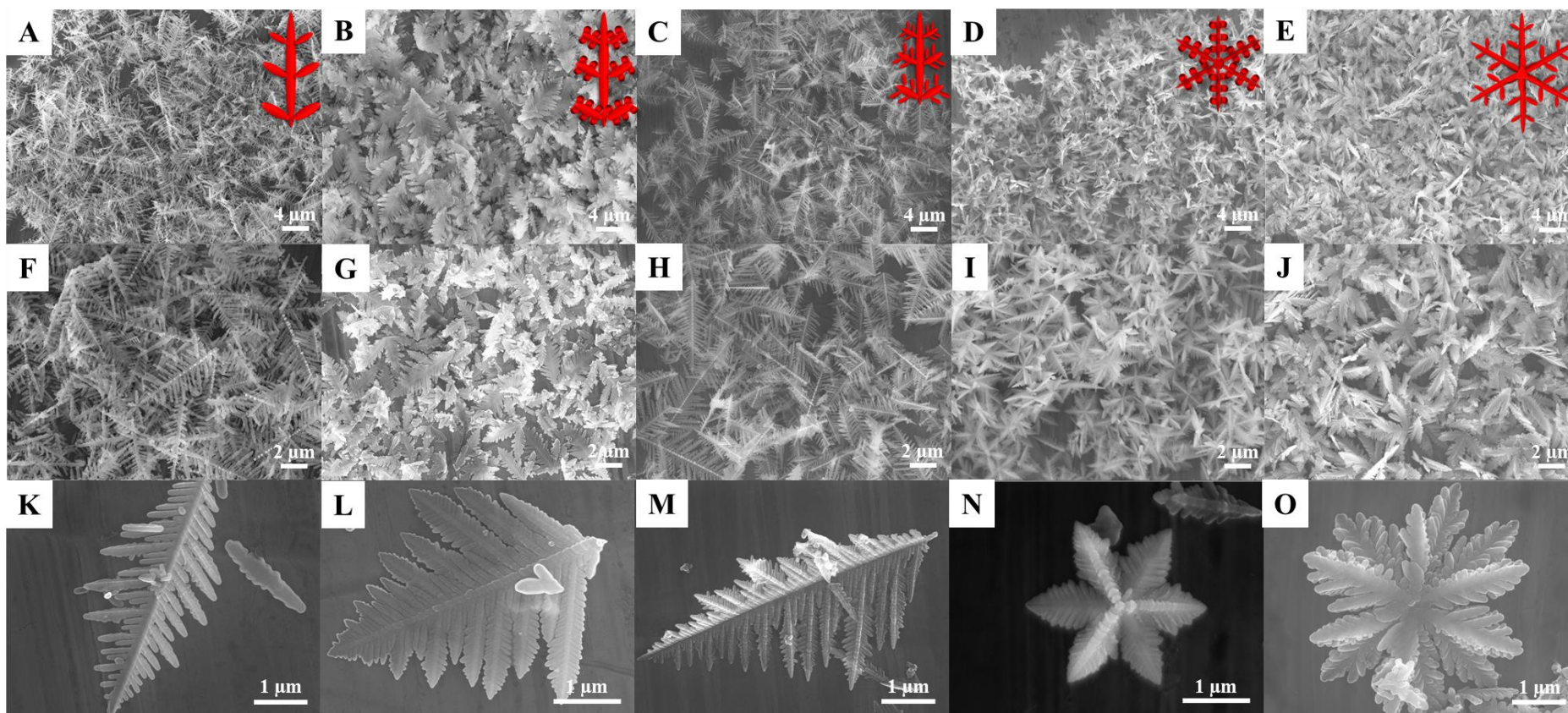


**Figure 2.2** (A-J) Low & (K-O) high magnification FE-SEM images of  $\alpha$ -Fe<sub>2</sub>O<sub>3</sub> fractal structures synthesized with a typical K<sub>3</sub>[Fe(CN)<sub>6</sub>] concentration of 4 mM at 180°C for 20 h. Sequential magnifications of the (A,F,K) *sec*B3D, (B,G,L) *tert*D2D, (C,H,M) *tert*D3D, (D,I,N) *sec*S2D and (E,J,O) *hyp*B2D images are scaled down correspondingly to the single particle image.

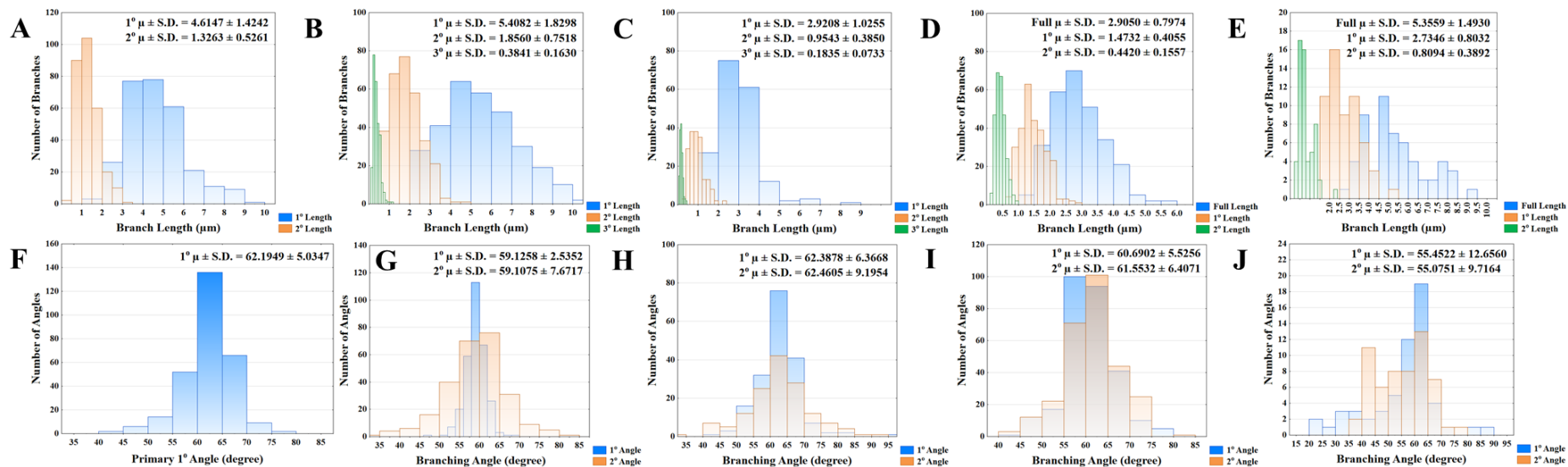


**Figure 2.3 (A-E)** Size and **(F-J)** angle distribution data of **(A,F)** *secB3D*, **(B,G)** *tertD2D*, **(C,H)** *tertD3D*, **(D,I)** *secS2D* and **(E,J)** *hypB2D* with a sample size of  $N = 300$ . *Exception*: Sample sizes of *tertD3D* and *hypB2D* are  $N = 180$  and  $60$ , respectively. *Top row*: The average “ $\mu$ ” lengths of primary “stem” (blue), secondary “branch” (orange) and tertiary “leaflet” (green) structural features, as calculated from individually measured particles, are symbolized by the  $1^\circ$ ,  $2^\circ$  and  $3^\circ$   $\mu$  lengths, respectively. The full average “ $\mu$ ” length (blue) is from the overall measured sizes of the flower-like *secS2D* and *hypB2D* structures. Thus, the corresponding  $1^\circ$  and  $2^\circ$   $\mu$  lengths symbolize the primary length (orange) and secondary branching (green) feature of the longest “petal”. *Bottom row*: The average “ $\mu$ ” angles between the primary “stem” and secondary “branch” (blue) as well as secondary “branch” with respect to the tertiary “leaflet” (orange) are symbolized by  $1^\circ$  and  $2^\circ$   $\mu$  angles, respectively. As for the flower-like structures, the  $1^\circ$  angle (blue) correspond to the median as chosen by measuring the angle between each “petal”. The  $2^\circ$   $\mu$  angle (orange) derived from the adjacent branched feature as measured by an angular displacement from the tip of the longest “petal”. *Note*: S.D. = Standard deviation calculated from a single variable, meaning  $N - 1$ .

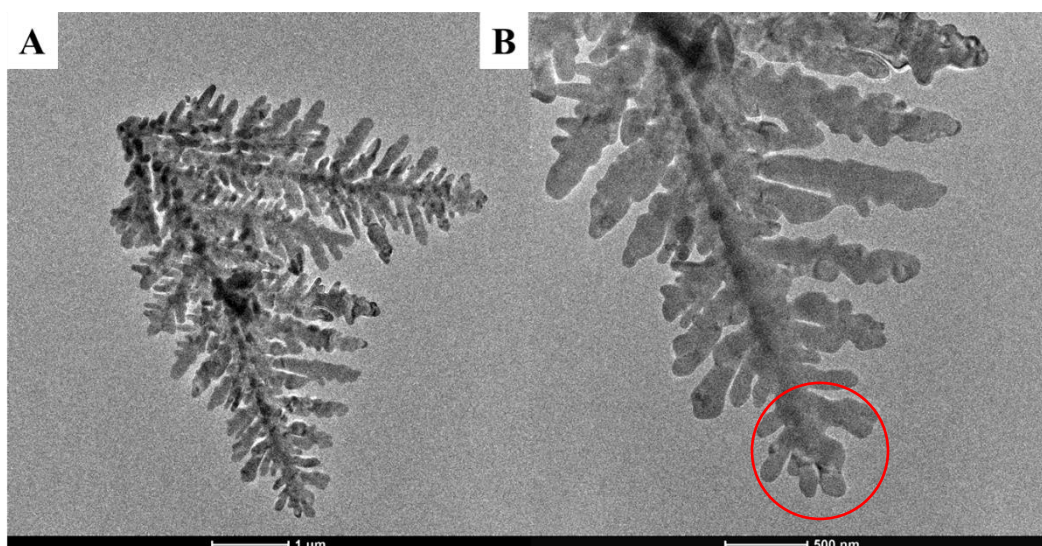


**Figure 2.4** (A) Low and (B) high magnification TEM images of an unusual *tertD2D* particle in the micron and submicron scales, respectively.

For the 3<sup>rd</sup> generation two-dimensional micro-dendrites (*tertD2Ds*), the average 1<sup>o</sup> “*stem*”, 2<sup>o</sup> “*branch*” and 3<sup>o</sup> “*leaflet*” lengths are 5.4082, 1.8560 and 0.3841  $\mu\text{m}$ , respectively (Fig. 2.3 B). The dispersity of the respective branch lengths of *tertD2Ds*, as defined by *CV*, was calculated to be 0.3383, 0.4051 and 0.4244, correspondingly. As expected, variations in size gradually increase from the 1<sup>o</sup> “*stem*” to 3<sup>o</sup> “*leaflet*” lengths, which further suggest that the surface hydrolysis of branching,<sup>51</sup> dominant at later stages of crystal growth as the case for reversed crystal growth, is subject to localized metal precursor concentration changes as also likely the case for *secB3Ds*. Similarly, the 1<sup>o</sup> and 2<sup>o</sup> branching angles (Fig. 2.3 G) were averaged to be 59.1258 and 59.1075 with *CV* values of 0.0429 and 0.1298, respectively. While the increasing variability in the branching angle may support our hypothesis of micro-strain effects, it remains a major challenge to probe such growth kinetics of specific facets, especially for the 2<sup>o</sup> “*branch*” and 3<sup>o</sup> “*leaflet*” as they are considered to be low energy facets, e.g. of  $\pm[10-10]$  and  $\pm[0-110]$ .<sup>48</sup> Due to the lack of instrumental standardization, it is an obvious fact that different

hydrothermal methods give rise to variations in the rate of heating in inorganic colloidal syntheses. To highlight our point, we demonstrated the morphological control of  $\alpha$ -Fe<sub>2</sub>O<sub>3</sub> branched crystals by simply changing the heating method while keeping other variables the same, as comparing with *secB3Ds* (Fig. 2.1).

In this case, pre-nucleation, which is the pre-emptive process to form thermodynamic nanoclusters of c.a. 1 – 3 nm,<sup>57</sup> was favoured through the gradual heating of the closed Teflon-lined reaction system. As such, we ensured the abundance of nucleation clusters for further assembly, most likely through oriented aggregation as discussed, at moderate temperatures of 140 – 160°C.<sup>22</sup> The major difference of this approach in synthesizing *tertD2D*, as compared to *secB3D*, is that there was more time allowed for pre-nucleation to the subsequent Ostwald ripening and aggregation processes. Due to such reasoning, we believe this is the cause of a wider primary size distribution (with 1° CV of 0.3383) as compared to *secB3D* (with 1° CV of 0.3086) (Fig. 2.3 A and B). Although low magnification images (Fig. 2.2 B & G) show that the batch consists almost entirely of *tertD2D* structures, fragments of micro-dendrites persist (Fig. 2.2 L) as common side products in pre-nucleation favoured reaction systems. Such fragments were not measured as part of the size distribution. Interestingly, using EtOH for the hydrolysis and condensation of  $\alpha$ -Fe<sub>2</sub>O<sub>3</sub> micro-dendrites has produced unusual assemblies of crystals (Fig. 2.4 A & B). Upon closer examination, we noticed that the tip of the dendrite seemed to grow multi-directionally, as reported in a prior study.<sup>52</sup> We speculated that this phenomenon of crystal growth was observed due to the pro-longed time which allows the mixed EtOH to vaporize and condense continuously via heat convection in the closed environment. More so, it is likely that this multi-branched particle was

not the result of fragmentation but by splintering at the terminal end. To exploit this unique phenomenon, we further synthesized *hypB2D* as would be discussed.

For the 3<sup>rd</sup> generation three-dimensional micro-dendrites (*tertD3Ds*), the average 1<sup>o</sup> “*stem*”, 2<sup>o</sup> “*branch*” and 3<sup>o</sup> “*leaflet*” lengths are 2.9208, 0.9543 and 0.1835  $\mu\text{m}$ , respectively (Fig. 2.3 C). As before, the dispersity of the respective branch lengths of *tertD3Ds*, as defined by *CV*, was calculated to be 0.3511, 0.4034 and 0.3995, correspondingly. Note that the size variations also follow an increasing trend from the 1<sup>o</sup> “*stem*” to 2<sup>o</sup> “*branch*”. Aside from the primary size distribution, however, the variations of the 2<sup>o</sup> and 3<sup>o</sup> features are about the same. Moreover, the 1<sup>o</sup> and 2<sup>o</sup> branching angles (Fig. 2.3 H) were averaged to be 62.3878 and 62.4605

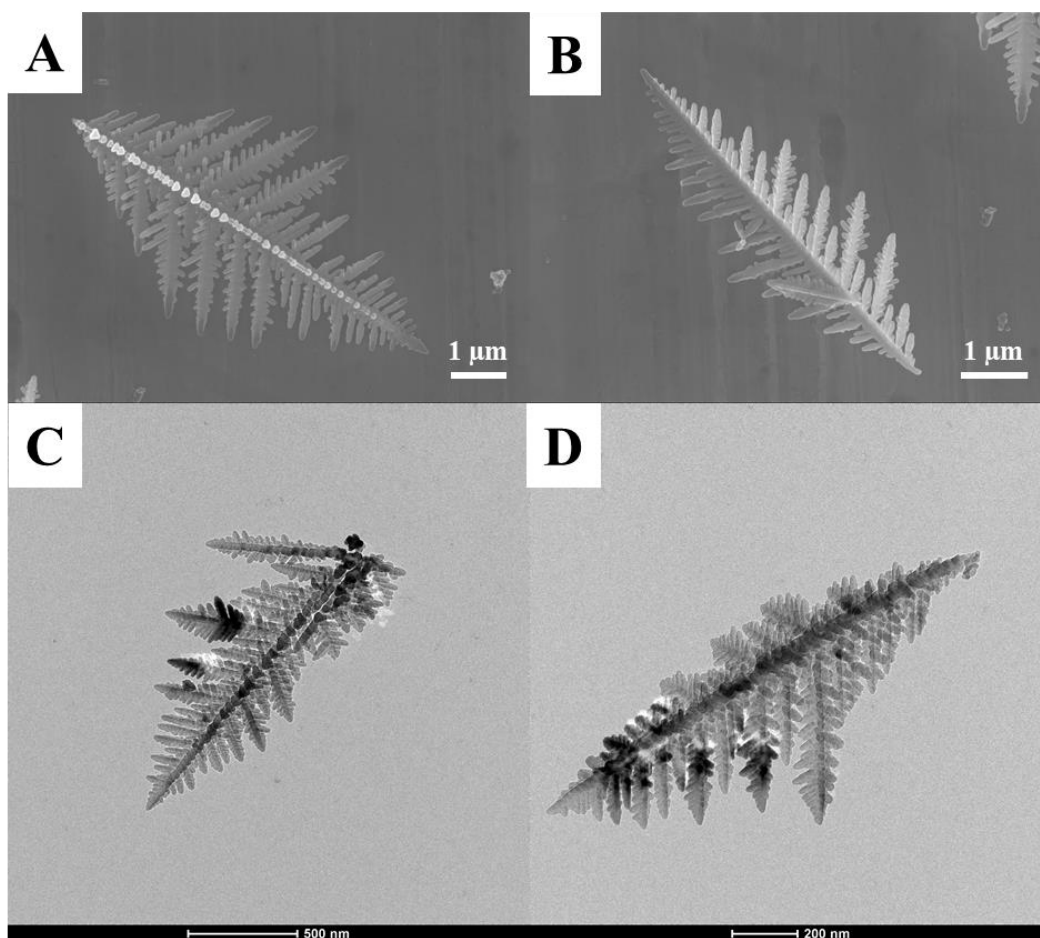


**Figure 2.5** Low magnification (A-B) FE-SEM and (C-D) TEM images, showing the (A,C) “back” and (B,D) “front” sides of typical *tertD3D* particles, respectively.

with *CV* values of 0.1021 and 0.1472, respectively. The variability of the 1° and 2° branching angles is clearly greater than that of the prior *secB3Ds* and *tertD2Ds* as described. *N,N*-dimethylformamide (DMF), our reaction solvent of choice, played a major role in the varied size and angular distributions for the synthesis of micro-dendrites. In fact, the solvent has always been valued for its chemical and thermal stability (with a boiling point at 153°C).<sup>58</sup> Moreover, its inherent polarity and wide solubility range for both organic and inorganic compounds reinforces itself as one of the most common solvents used in the synthesis of metal organic frameworks (MOFs).<sup>53</sup> Besides, it also commonly acts as a mild reducing agent for soft noble metal colloids, such as gold and silver. In this case, DMF was not added as a reducing agent as the metal Fe<sup>3+</sup> cation has a comparatively lower standard redox potential (Fe<sup>3+</sup> + e<sup>-</sup> ↔ Fe<sup>2+</sup>;  $E^0 = 0.771$  at 25°C vs. NHE), meaning it does not reduce readily even at hydrothermal conditions. As a result, our choice of the solvent lies mainly in the lower viscosity ( $\eta = 0.82$  mPa·s at 20°C) as well as its chemical and thermal stability as mentioned. On the other hand, both H<sub>2</sub>O and EtOH are known to have higher viscosities ( $\eta = 1$  and 1.153 mPa·s, respectively, at 20°C). It was suggested that the lower viscosity likely plays a major role in assisting the migration of nuclei for the respective self-assembly of the micro-dendrites in later growth stages. A similar study has also suggested an elegant solution by simply increasing the hydrocarbon chain length of an alcohol, such as by using 1-butanol instead, could facilitate favourable processes of oriented aggregation.<sup>59</sup> In addition, the high thermal stability (with a specific heat capacity,  $C_p = 146.05$  J/K·mol) of DMF could potentially reduce the nucleation rate, as compared to H<sub>2</sub>O and EtOH, in the primary nucleation stage. Thus, it is more likely that nucleation took place more slowly and uniformly than the case of *tertD2D*. As a result, we observed less variability in the

2° and 3° length distributions whereas the branching angles of 1° and 2° varied more. Such could mean that uniformly formed small-sized nuclei, in the H<sub>2</sub>O-to-DMF mixture, orient themselves and attach via lattice matching.<sup>22</sup>

To our knowledge, this is the first time such small-sized (2 – 4 μm) dendritic α-Fe<sub>2</sub>O<sub>3</sub> micro-crystals were obtained in such high yield and uniformity (Fig. 2.2 C & H). By comparing with the literature, the typical sizes of the dendritic micro-crystal, as defined by the length of the trunks, were reported to range from 3 to 6 μm.<sup>22</sup> In one particular study,<sup>17</sup> the length of the dendritic trunk can even be as long as 15 μm, which is probable according to our experience. Certainly, the overall particle sizes vary with the precursor concentration and aging time (Fig. 2.12). As such, we suspect that even smaller sized dendritic α-Fe<sub>2</sub>O<sub>3</sub> micro-crystals may be obtained if the precursor concentration used were to be lowered, K<sub>3</sub>[Fe(CN)<sub>6</sub>] < 4 mM. Nonetheless, the morphological features of *tertD3D* remained similar to those reported as dendritic “micro-pine” or “feature-like” α-Fe<sub>2</sub>O<sub>3</sub> structures.<sup>22</sup> Briefly, the single crystal (Fig. 2.2 M) shows the “front” side of the *tertD3D*, where brighter regions (to the *left*) represent the edges while the dark regions (on the *right*) represent the recesses, which are lying parallel along the horizontal plane. As a result, we confirm that *tertD3D* is also three-dimensional. As the *tertD2D*, *tertD3D* also has both “front” and “back” sides (Fig. 2.5). As revealed by the “back” side (Fig. 2.5 A), the single crystal features triangular (“pyramid-like”) corrugations along the pronounced trunk. Further interrogation via the TEM image (Fig. 2.5 C) shows that the corrugations are indeed organized periodic features with the tip of the triangle pointing towards the protrusion or primary growth direction. The sizes of the triangular corrugations were individually measured and averaged to be

around  $46 \pm 4$  nm, which is approximately four times smaller than the typically reported size of 200 nm.<sup>50</sup> The “darkened” corrugations as observed (Fig. 2.5 C) seem to suggest that the triangular features were either grown or attached onto the pre-existing trunk. Furthermore, the “brightness” of the corrugations (Fig. 2.5 A) suggests that the highly ordered parallel  $2^\circ$  *branches*, distributed on both sides of the trunk, seems to be protruding anchors lifting the corrugations up. Although the geometry deduces that the combined  $1^\circ$  branching angles (between the two  $2^\circ$  *branches* on both sides) are approximately  $120^\circ$ , consistent with the rhombohedral structure, the full three-dimensional parameters of the single crystal remain unclear as only the two-dimensional representations can be visualized here. On the other hand, the “front” side images (Fig. 2.5 B & D) are consistent with the representation (Fig. 2.2 M) as discussed. Further probing (Fig. 2.5 D) reveals that, aside from being a three-dimensional single crystal, the individual  $2^\circ$  *branches* feature miniscule nanoparticles along its surface. These oriented nano-features were also individually measured and averaged to be around  $16 \pm 2$  nm, around five times smaller than the typically reported size of 100 nm.<sup>50</sup> Through qualitative comparison, we conclude that these miniscule features are more obvious at the “front”. Previous study has ascribed these hierarchical dendrites as single crystals via selective area electron diffraction (SAED),<sup>22</sup> meaning the different fractals’ lattices match each other with an almost perfect crystallographic order. Certainly, this highly depends on the orientation of the crystal arranged via the tilting angle on the sample grid. Unlike *tertD3D*, on the other hand, *tertD2D* would most likely not reveal an ideal single crystal pattern due to its poor crystallinity. This raises further contemporary questions (*not tackled in this thesis*): (1) How did the  $2^\circ$  *branch* and  $3^\circ$  *leaflet* arrange via lattice matching? (2) Did that process occur consecutively or

concurrently? (3) If crystallographic order were to be so important, how did *tertD2D*'s hierarchical features recognize each other and arrange themselves?

For the “starfish-like” two-dimensional micro-dendrites (*secS2Ds*), the average “*full*”, 1° “*stem*” and 2° “*branch*” lengths are 2.9050, 1.4732 and 0.4420  $\mu\text{m}$ , respectively (Fig. 2.3 D). The dispersity of the respective *overall*, *stem* and *branch* lengths of *secS2Ds*, as defined by *CV*, was calculated to be 0.2745, 0.2753 and 0.3523, correspondingly. The variations in size distribution remained the same for the particle's *overall* and 1° *stem* length, except for the 2° *branch*. The 1° and 2° branching angles (Fig. 2.3 I) were averaged to be 60.6902 and 61.5532 with *CV* values of 0.0910 and 0.1041, respectively. The variability of the 1° and 2° branching angles is considerably lower than that of *tertD3Ds*. Low magnification images (Fig. 2.2 D & I) seem to reveal highly uniform sizes of *secS2Ds*, with lower *CV* values. Our optimized synthetic method is a significant improvement to that of a previously reported study.<sup>40</sup> Octylamine ( $\text{C}_8\text{H}_{19}\text{N}$ ) was suggested as an inhibitory agent to favour the growth directions from  $\langle 11-20 \rangle$  to  $\langle 10-10 \rangle$ , thereby facilitating the morphological evolution from the typical “snowflake” to “starfish”.<sup>40</sup> Here, ammonia ( $\text{NH}_3$ ) was added as the basic catalyst, which eventually forms ammonium hydroxide ( $\text{NH}_4\text{OH}$ ) via hydrolysis. This condition is further supported by the measurement of pH (see *insert* of Fig. 2.1). At first glance, non-aqueous solvents seem to contribute to the lower pH in the bulk; however, the effects were less pronounced and insignificant as compared to the case of *secS2Ds*. This approach is based on the concept of surface potential to drive the selective crystal growth via the Lewis acid sites on the  $\{11-20\}$  surfaces, which is facilitated by the surface hydrolysis of the  $[\text{Fe}(\text{CN})_6]^{3-}$  anions.<sup>51</sup> Due to the insolubility of  $\text{C}_8\text{H}_{19}\text{N}$  in an

aqueous medium, 1-propanol (1-PrOH) was also added, for an optimized H<sub>2</sub>O-to-1-PrOH ratio of 4 : 1, to assist in the dissolution at ambient conditions. The choice was justified as 1-PrOH was previously reported to assist in oriented aggregation.<sup>59</sup> During our synthesis, we have found 1-PrOH to yield the best result among other solvents, such as ethanol (EtOH), isopropyl alcohol (IPA), and 1-butanol (1-BuOH), added to create an aqueous-organic mixture. Thus, the optimized medium was designed to obtain the most desirable outcome of a highly uniform batch of microcrystals, by maximizing the solubility of all the chemical components involved at the initial stage. Interestingly, the overall calculated average sizes of *tert*D3Ds and *sec*S2Ds are very similar (Fig. 2.3 C & D). This suggests to us that, in a basic environment, the growth rate of <11-20> must be quite slow with C<sub>8</sub>H<sub>19</sub>N, as verified by prior studies.<sup>40</sup> While a reduction in nucleation rate may also play a role, as in the case of *tert*D3D, it is likely not the major variable in this synthesis.

To our knowledge, this is the first attempt to re-evaluate the “structure-to-activity” relationship with {11-20} facets of these “starfish-like”  $\alpha$ -Fe<sub>2</sub>O<sub>3</sub> microdendrites, denoted here as *sec*S2Ds. This is so despite prior facet-dependent studies claiming that  $\alpha$ -Fe<sub>2</sub>O<sub>3</sub> crystals with predominately exposed {10-10} facets should possess a higher photocatalytic activity.<sup>65</sup> From a morphological standpoint, the single particle image (Fig. 2.2 N) reveals that the crystal seems to follow six-fold symmetry as growth is symmetric along the six crystallographically equivalent <11-20> directions. This representation resembles the typically reported “snowflake-like”  $\alpha$ -Fe<sub>2</sub>O<sub>3</sub> morphologies, which its crystalline structure is instead defined by the six equivalent <10-10> directions:  $\pm[10-10]$ ,  $\pm[1-100]$  and  $\pm[0-100]$ , as lower energy facets of the hexagonal crystal lattice.<sup>48</sup> Careful examination, however,

shows the adjacent 1° *stems* differ as tiny “pyramid-like” nanoparticles (size of  $81 \pm 9$  nm) arrange themselves at the “back” of three out of six protrusions. Therefore, the overall crystal geometry seems to agree with a three-fold symmetry, resembling the rhombohedral crystal lattice. Interestingly, closer inspection at the center of the *secS2D* particle shows that two of the triangular or “pyramid-like” nanoparticles were fused together into a hexagonal core structure. However, further probing of the inner structure (Fig. 2.6 A & C) with another selection of particles did not reveal such uniform and unique feature, which suggests that this may just be a singular occurrence. On the contrary, the existence of nanopores ( $d = 26 \pm 3$  nm, measured diagonally) on *secS2Ds* (Fig. 2.6 B & D) seem to be relatively common. As the individual 1° *stems* are similar in length, we believe that the *secS2Ds* are lying alongside the horizontal plane. Thus, justifying as two-dimensional in nature.

For the “hyper-branched” two-dimensional micro-dendrites (*hypB2Ds*), the average “*full*”, 1° “*stem*” and 2° “*branch*” lengths are 5.3559, 2.7346 and 0.8094  $\mu\text{m}$ , respectively (Fig. 2.3 E). The dispersity of the respective *overall*, *stem* and *branch* lengths of *hypB2Ds*, as defined by *CV*, was calculated to be 0.2788, 0.2937 and 0.4809, correspondingly. As in *secB3Ds* and *tertD2Ds*, the size distribution variations follow an increasing trend in the order of the particle’s *overall*, 1° *stem* length, and to 2° *branch*. The 1° and 2° branching angles (Fig. 2.3 J) were averaged to be 55.4522 and 55.0751 with *CV* values of 0.2282 and 0.1764, respectively. Note here that both size and angular distributions depict as bi-modal distributions. Indeed, low magnification images (Fig. 2.2 E & J) reveal more randomly sized distributions of *hypB2Ds*. Unlike *secS2Ds*, *hypB2Ds* do not possess any specific geometry as suggested by the greater deviation in angular distributions. Rather, the selection of

a non-fragmented crystal (Fig. 2.2 O) seems to suggest that it consists of two “back-to-back” layers of the sixfold-symmetric crystal, creating a “flower-like” structure with a maximum of twelve petals. While the abundance of fragments is likely due to pre-nucleation (as in the case of gradual heating to form *tert*D2Ds), the double-layered phenomenon could occur due to the simple fact that the “mesh-like” precursor of  $K_3[Fe(CN)_6]$  is sparsely soluble in EtOH. Due to the proximity between two separate nuclei, it is not unlikely that double-layered snowflake structures may form merely due to the closeness in inter-nuclei distance, which may also be the case in a prior study using polyethylene glycol ( $M_w = 4000$ ) as the surfactant.<sup>48</sup> An alternative explanation was provided by another study which showed that, indeed, double-layered structures could be formed under high pH ( $> 12.0$ ) and a prolonged aging time ( $> 12$  h).<sup>52</sup> However, our synthetic method of choice was neither reacted at a sufficiently basic nor prolonged reaction condition (see Fig. 2.1). This has led us to believe that our double-layered crystal (Fig. 2.2 O) is the result of proximity of separate crystalline nuclei during the hydrothermal reaction. In attempt to support this hypothesis, we have purposefully added more EtOH into the Teflon-lined reaction vessel, reaching a  $H_2O$ -to-EtOH bi-solvent ratio of 1 : 3. Surprisingly, hexagon-shaped micron-sized platelets (Fig. 2.7 A) were formed instead. Closer examination (Fig. 2.7 B) shows the micro-plates’ surfaces are arranged by nano-sized hexagonal platelets ( $d = 216 \pm 44$  nm). Due to the uniformity in size distribution of both structures (Fig. 2.2 O & 2.7 A), as observable at all sides of the single particle (Fig. 2.7 B), the obtained products are two-dimensional in nature. Although we were not able to confirm our hypothesis, it is obvious that solvent effects have significant implications on the yielded outcome of morphology. This has led us to explore more in our subsequent discussions.

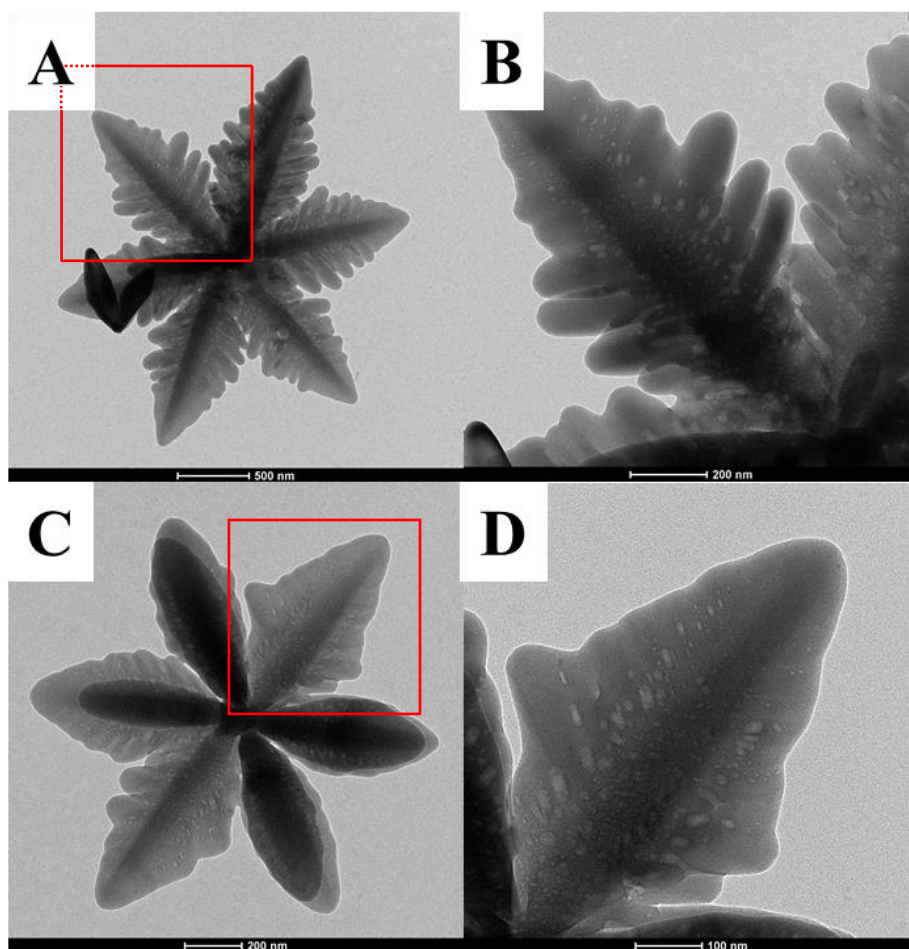


**Figure 2.6** (A,C) Low and (B,D) high magnification TEM images of typical *secS2D* particles showing a (A) normal and (C) stacked variant, respectively, in the submicron scale.

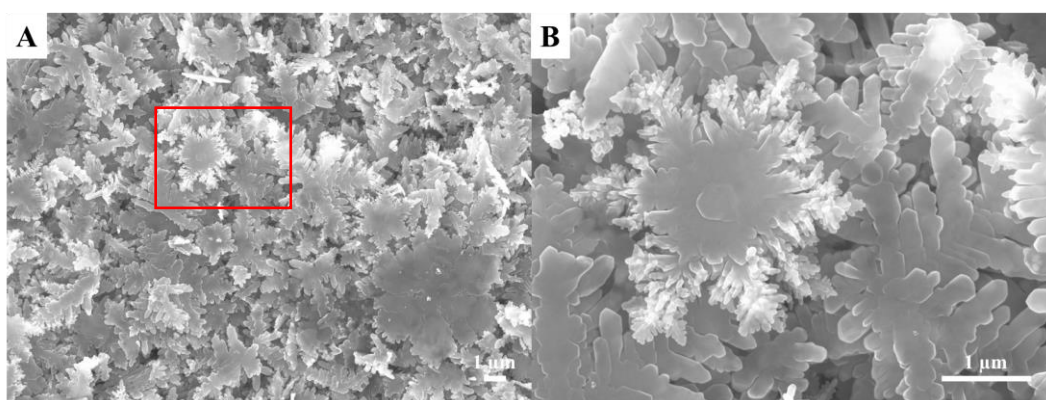


**Figure 2.7** (A) Low and (B) high magnification FE-SEM images of typical *hypB2D* particles (as major product) in  $H_2O:EtOH$  bi-solvent ratio of 1 : 3 at the micron scale.

**Structural and Vibrational Information Analysis.** Profile matching of *p*XRD patterns not only provides information on the crystalline structure, but also determines the degree of crystallinity, which justifies sample purity. All diffraction peaks of the as synthesized micro-dendrites (Fig. 2.8) can be indexed to the pure rhombohedral phase of  $\alpha$ -Fe<sub>2</sub>O<sub>3</sub> (*hematite*; space group *R-3c*), which is in good agreement with the literature values ( $a = 5.035$ ,  $c = 13.740$  Å, JCPDS # 33-0664). Note that the XRD peaks may be labelled by the three- and four-index systems (Fig. 2.11 C), as for hexagonal nanostructure. Hematite has a rhombohedral-centered hexagonal (corundum-type) structure with a close-packed oxygen lattice in which two-thirds of the octahedral sites are occupied by Fe<sup>3+</sup> ions. Typically, the sharpness (intensity) of the diffraction peaks suggests varied degrees of crystallinity, whereas the narrowness (width) suggests varied crystallite sizes in the branched  $\alpha$ -Fe<sub>2</sub>O<sub>3</sub> samples. According to the Ruland method, by taking the integral of crystalline peaks over the total area, the extent of crystallinity for *secB3D*, *tertD2D*, *tertD3D*, *secS2D*, and *hypB2D* were determined to be 96.0, 94.3, 99.5, 89.6, and 96.7 %, respectively. Overall, the absence of other residual peaks suggests all the products were obtained at relatively high purity. Despite the prevalence of fragmented crystallites in *tertD2D* and *hypB2D*, surprisingly, *secS2D* is the least crystalline of all. Furthermore, the average crystallite size (“*D*-value”) of *secB3D*, *tertD2D*, *tertD3D*, *secS2D*, and *hypB2D* were determined to be 74, 71, 65, 72, and 61 nm, respectively, via the Scherrer equation. While interplanar distance (“*d*-spacing”) may also be calculated, it is irrelevant here as observing lattice fringes is beyond our means with the performance of the TEM available to us.

Vibrational analyses of inorganic solid-state structures not only provide

information on the organic constituents residing on the surface of the crystal, but also verifies the formation of desirable mineral phases via the identification of characteristic peaks. The distinguished (strong), also broad, FTIR absorption peaks of the as synthesized micro-dendrites (Fig. 2.9 A) are in the range of 400 to 900  $\text{cm}^{-1}$ , which are from the inherent lattice vibrations of the  $\alpha\text{-Fe}_2\text{O}_3$  phase, verifying our *p*XRD results. As previously suggested,<sup>67</sup> there are a total of six infrared active modes for  $\alpha\text{-Fe}_2\text{O}_3$  lattice vibrations: two polarized along the *c*-axis ( $\parallel$  modes), and four perpendicular to the *c*-axis ( $\perp$  modes). The absorptions at 435 and 519  $\text{cm}^{-1}$  are ascribed to the  $\perp$  mode while that at 646  $\text{cm}^{-1}$  to  $\parallel$  mode, in agreement with an early work by Chen *et al.*<sup>67</sup> To our knowledge, another higher frequency peak at 795  $\text{cm}^{-1}$  was neglected by prior studies which is likely of  $\parallel$  mode. However, the reason for the high frequency peak's disappearance in *sec*S2D is unknown. Similarly, the weak absorption at 646  $\text{cm}^{-1}$  ( $\parallel$  mode) was not observed in the case of *tert*D3D.

Originally, we have conducted FTIR analyses to evaluate any remaining presence of organic residues, especially octylamines, on the surfaces of *sec*S2Ds. As expected, no notable N-H bending vibration of primary amines (1580 – 1650  $\text{cm}^{-1}$ ), as present in terminal  $\text{-NH}_2$  groups, was observed (Fig. 2.9 B). This suggests that none of the primary amines persist after extensive rinsing of the catalyst. Interestingly, after thermal decomposition (Fig. 2.10), *sec*S2Ds showed a weight loss of 6.19 % at the onset of 77.8°C, ending at 203.7°C. Consequently, unknown peaks at 1738 and 2342  $\text{cm}^{-1}$  were observed. To investigate this further, we have analyzed our samples via XPS and subsequently conducted elemental composition analyses for *sec*S2Ds before and after thermal decomposition. Unfortunately, we did not yield any useful information from this study.

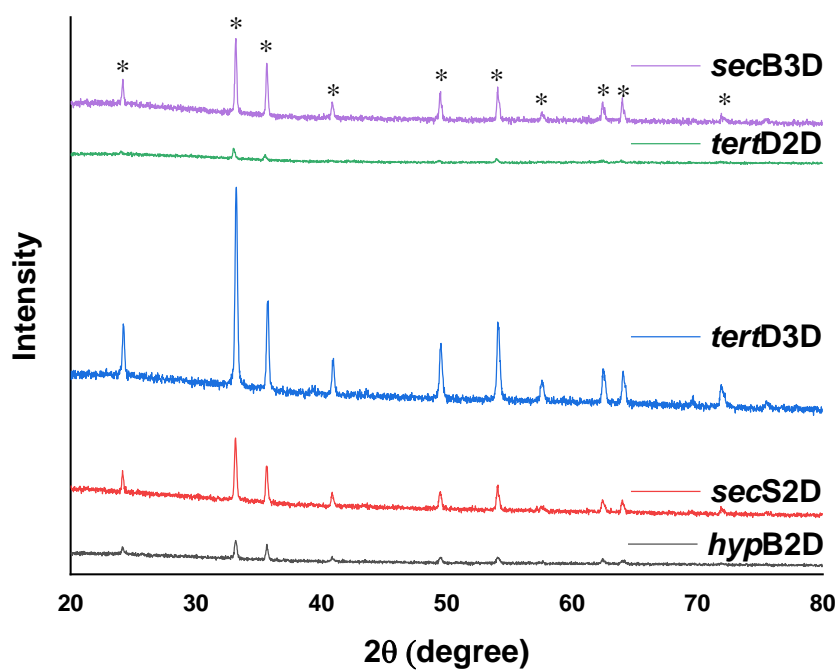


**Figure 2.8** pXRD patterns of *secB3D* (purple), *tertD2D* (green), *tertD3D* (blue), *secS2D* (red) and *hypB2D* (black), matching closely to that of pure  $\alpha$ - $\text{Fe}_2\text{O}_3$  phase (JCPDS 33-0664).

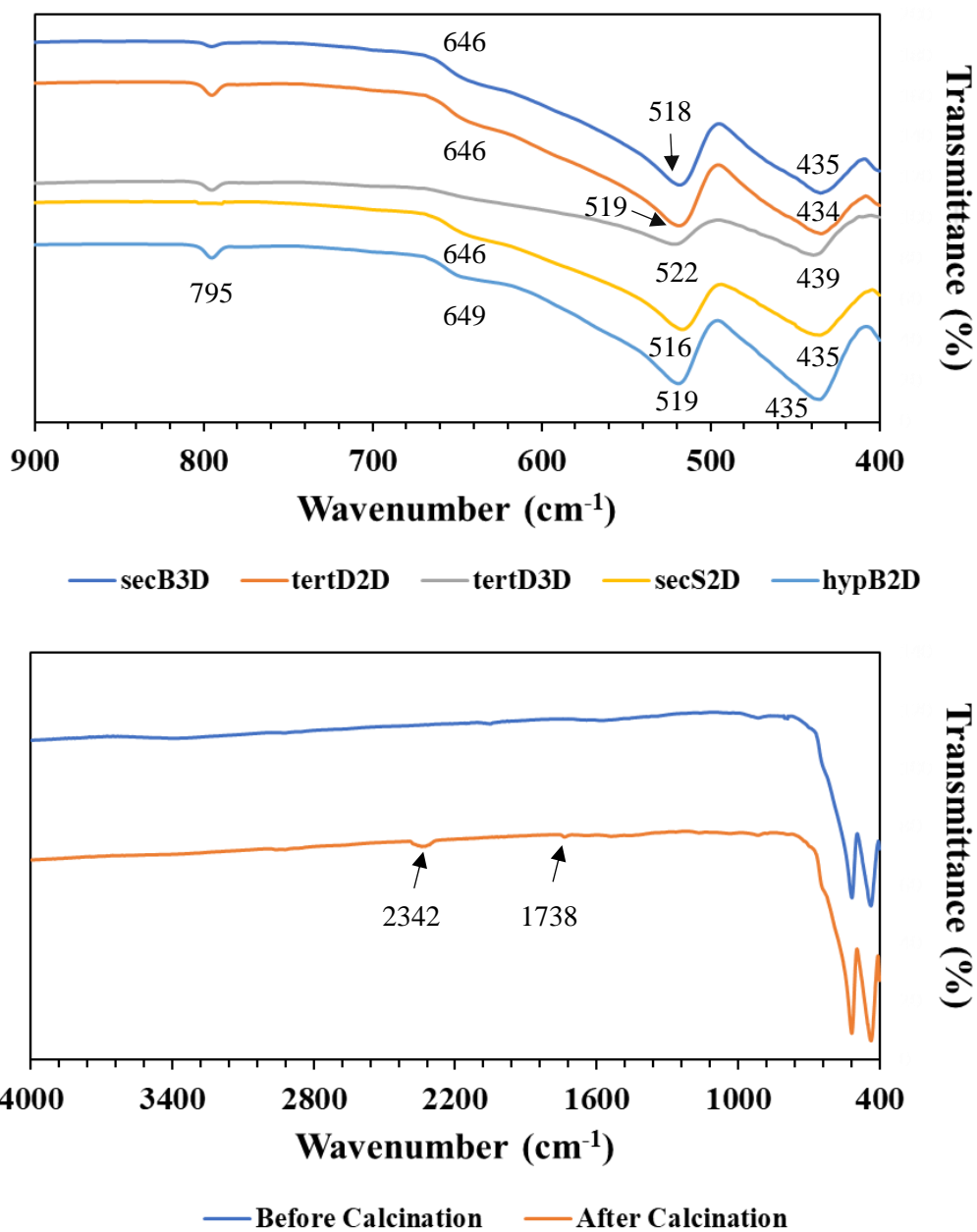


**Figure 2.9** FTIR spectra of the (A) as synthesized dendritic microparticles, namely *secB3D* (ocean blue), *tertD2D* (orange), *tertD3D* (grey), *secS2D* (yellow) and *hypB2D* (sky blue), and (B) *secS2D* before (blue) and after calcination (orange) from 40 to 900°C (40°C/min).

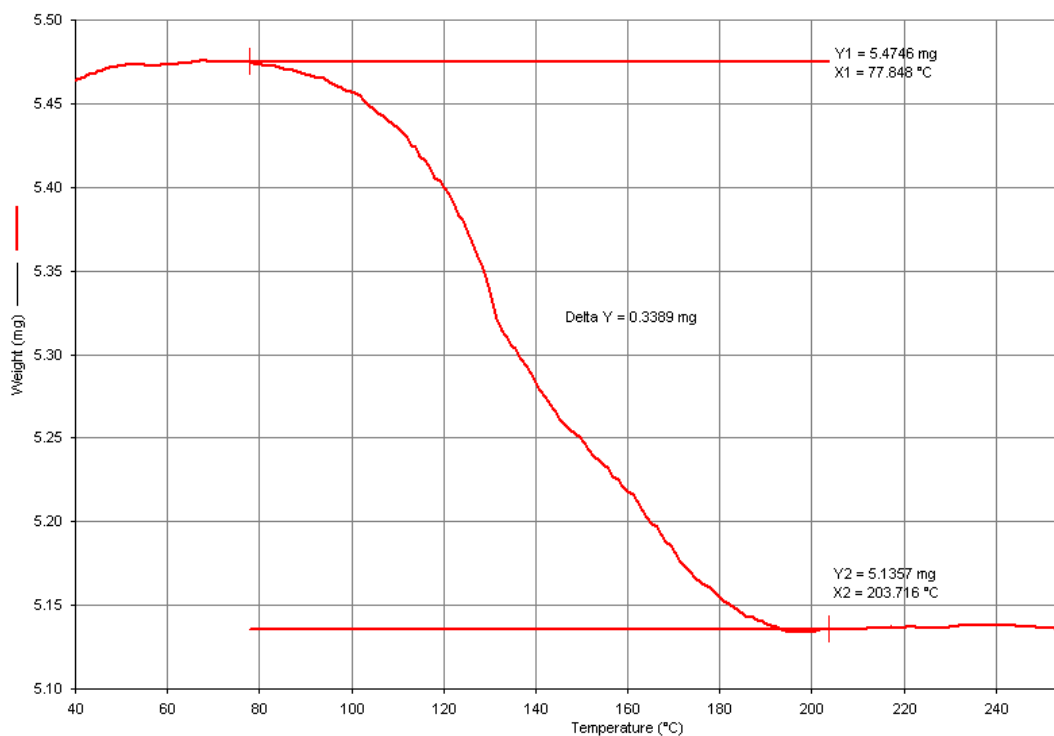


**Figure 2.10** TGA diagram of *secS2D* showing the onset (X1, Y1) and offset (X2, Y2) points of a thermal transition curve, which ranges from the initial temperature at 40 to 260°C.

**Growth Mechanism of Typical Dendritic Hematite.** As the synthesis of dendritic or branched  $\alpha$ -Fe<sub>2</sub>O<sub>3</sub> particles is sensitive to localized precursor concentrations, we have investigated this via changing the metal concentration and aging time. By increasing the concentration, thicker and larger  $\alpha$ -Fe<sub>2</sub>O<sub>3</sub> fractals were obtained at high yield and uniformity via the hydrothermal synthesis of 38 mM K<sub>3</sub>[Fe(CN)<sub>6</sub>] at 180°C for 20 h (Figure 2.11 A). High magnification (Fig. 2.11 B) of these products reveal the presence of pseudo-cubic crystals as well as the thickened and enlarged dendritic  $\alpha$ -Fe<sub>2</sub>O<sub>3</sub> crystals. The distinguished peak for the (104) facet (Fig. 2.11 C) further supports the presence of these rhombohedral crystals. A closer inspection of a single structure (Fig. 2.11 D), with the axes aligned with the anisotropic growth directions of [10-10], [0-110] and [1-100], reveals the preservation of the *hcp* geometry as the angles were measured to be 60°.

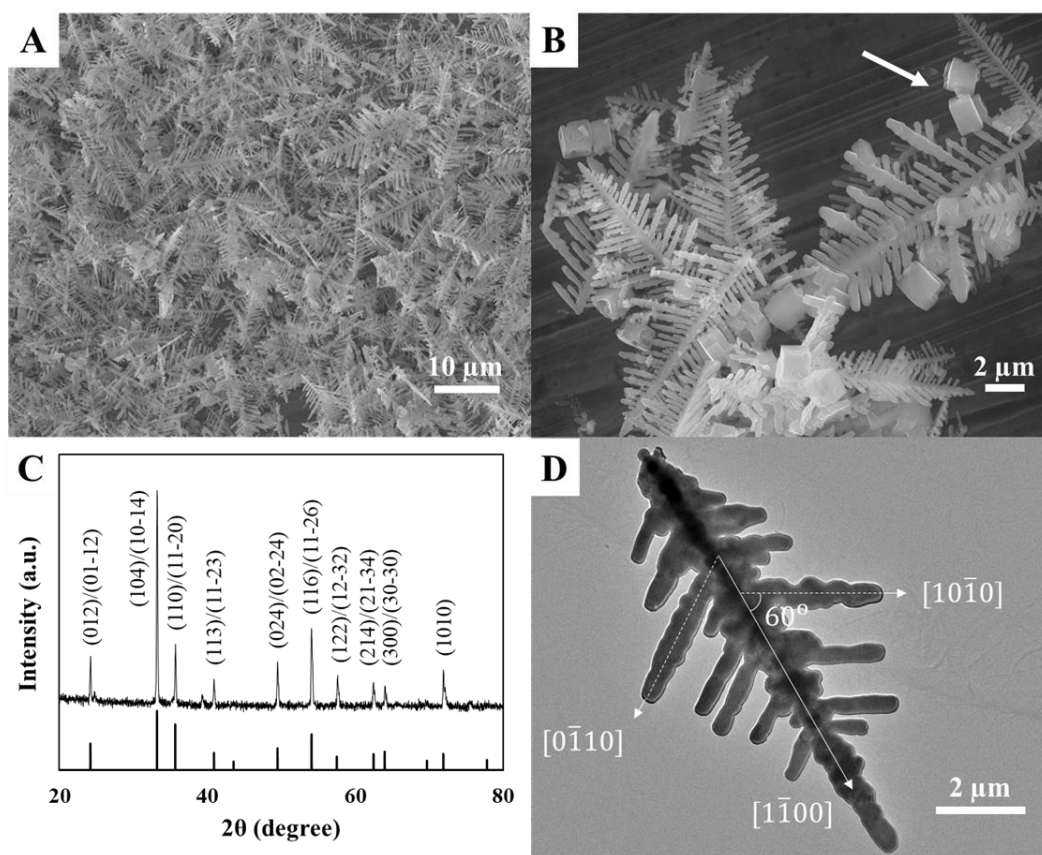


**Figure 2.11** (a) Low and (b) high magnification FE-SEM images of branched  $\alpha$ - $\text{Fe}_2\text{O}_3$  fractals synthesized with a  $\text{K}_3[\text{Fe}(\text{CN})_6]$  concentration of 38 mM at  $180^\circ\text{C}$  for 20 h. (c) *p*XRD pattern of the sample confirming formation of a pure  $\alpha$ - $\text{Fe}_2\text{O}_3$  phase (JCPDS 33-0664). (d) Low magnification TEM image showing the angle between the corresponding anisotropic growth directions.

Synthetic parameters, such as concentration and aging time (as mentioned), were effective in tuning the overall size and shape of the dendritic  $\alpha$ - $\text{Fe}_2\text{O}_3$  particles. Synthesized structures by hydrothermal treatment were varied from 3.8 to 38 mM  $\text{K}_3[\text{Fe}(\text{CN})_6]$  and 8.0 to 20 h at a fixed temperature of  $180^\circ\text{C}$  (Figure 2.12). As expected, increasing the concentration from 3.8 to 38 mM facilitated the synthesis of larger and thicker branched  $\alpha$ - $\text{Fe}_2\text{O}_3$  crystals (Figure 2.12 A, B & C, D). Interestingly, it is notable that the overall sizes of the dendritic  $\alpha$ - $\text{Fe}_2\text{O}_3$  crystals did not increase significantly at the lower concentration of 3.8 mM as the reaction time was varied from 8 to 20 h (Fig. 2.12 A & C). Meanwhile, at the fixed concentration

of 38 mM, enlarged dendritic  $\alpha$ -Fe<sub>2</sub>O<sub>3</sub> crystals seemed to have reduced in size instead as reaction progresses (Fig. 2.12 B & D). Furthermore, at a shorter aging time of 8 h (Fig. 2.12 C), tertiary 3° dendritic  $\alpha$ -Fe<sub>2</sub>O<sub>3</sub> (known as “feather-like”) micro-crystals, similar in morphology to *tertD3Ds*, have grown. Unfortunately, the yields obtained in mass for the dendritic  $\alpha$ -Fe<sub>2</sub>O<sub>3</sub> at 8 h were too low for use. Although morphological evolution was possible simply by changing the reaction parameters, concentration and aging time, to vary the overall size and shape of dendritic  $\alpha$ -Fe<sub>2</sub>O<sub>3</sub>, we did not deem this traditional method worthy to obtain the high yields and uniformly necessary for applications in heterogeneous catalysis. Similar studies have been conducted prior to our own.<sup>22</sup>

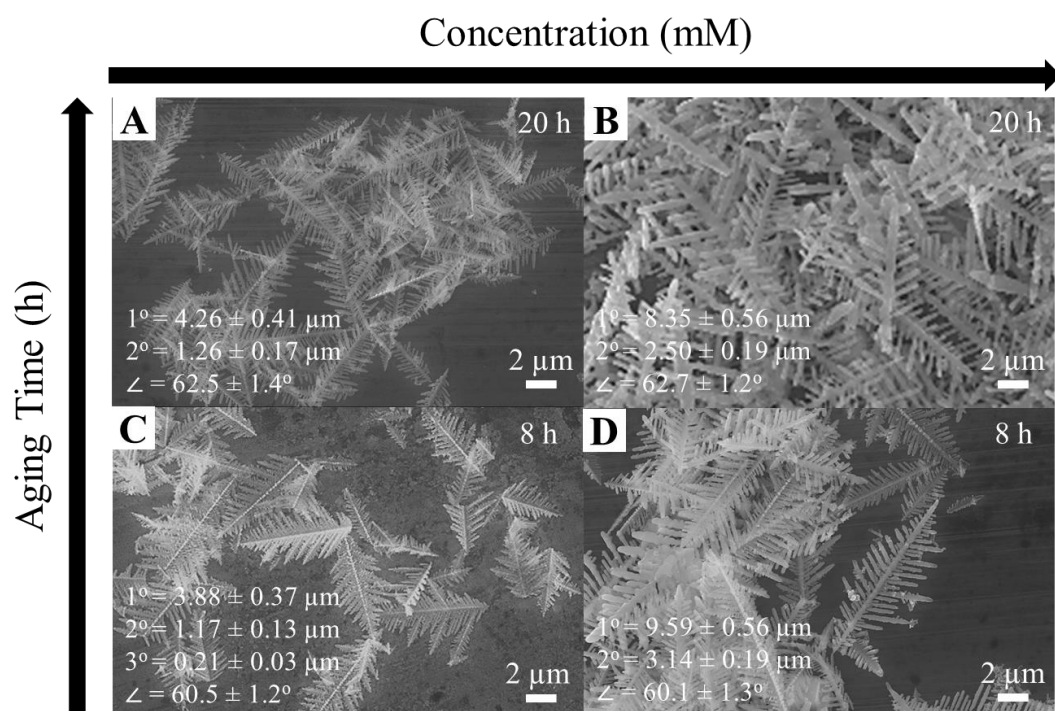


**Figure 2.12** Low magnification FE-SEM images of  $\alpha$ -Fe<sub>2</sub>O<sub>3</sub> fractal structures synthesized with a K<sub>3</sub>[Fe(CN)<sub>6</sub>] concentration of (C,A) 3.8 mM and (D,B) 38 mM at 180°C for 8 and 20 h (bottom and top), respectively. The average lengths of the 1° “stem”, 2° “branch” and 3° “leaflet” were calculated out of  $N = 100$  particles (Sample A, B, C and D). The symbol “ $\zeta$ ” refers to the angle between 1° and 2° anisotropic growth directions. Standard error of the single variables (with  $N - 1$ ) were further calculated based on a 95% confidence level.

As heating methods differ between different studies (as also mentioned), we decided to conduct our own time-dependent crystal growth studies (Fig. 2.13 & 2.14). Briefly, separately obtained  $\alpha$ -Fe<sub>2</sub>O<sub>3</sub> dendritic samples, as synthesized via the hydrothermal treatment of 3.8 mM K<sub>3</sub>[Fe(CN)<sub>6</sub>] at 180°C, were aged at varied reaction times, namely (A) 1.5, (B) 2.0, (C) 3.0, (D) 4.0 and (E) 8.0 h (Fig. 2.13). As observed, the surface hydrolysis and crystallization of [Fe(CN)<sub>6</sub>]<sup>3-</sup> anions seem to occur relatively quickly within 1.5 h. At 2 h, distinguishable features of the  $\alpha$ -Fe<sub>2</sub>O<sub>3</sub> micro-dendrites become clearly visible while small spherical nuclei existed in the background. Further to 3 h, dendritic fragments were prevalent, indicating the incomplete formation of our product. Interestingly, the “*feather-like*”  $\alpha$ -Fe<sub>2</sub>O<sub>3</sub> dendrites formed, which were seemingly larger and more fibrous, as the major product at 4 h. At 8 h, the desirable product, similar in morphology to *tert*D3D (as mentioned in Fig. 2.12 C), was obtained. The corresponding crystallite (grain) sizes (Fig. 2.13 F), parameter “*D*” in the Scherrer equation, were calculated via the time-dependent *p*XRD patterns (Fig. 2.14) obtained from the aging time of 2 to 48 h. As indicated by the obvious reduction in crystallite size at 12 h, there was a trend of dissolution-recrystallization (shown by the *parabola* opening upwards), as also previously confirmed by our morphological studies under SEM (*data not shown*). To our knowledge, this is the first time the dissolution-recrystallization mechanism was shown quantitatively in a time-dependent manner for the crystal growth studies of dendritic  $\alpha$ -Fe<sub>2</sub>O<sub>3</sub> micro-crystals. Despite the similarity in crystallite sizes at the early stage of growth between 2 to 4 h (Fig. 2.13 B to D), the crystallite size seemed to have increased from the evolution of largely fibrous to the smaller “*feather-like*”  $\alpha$ -Fe<sub>2</sub>O<sub>3</sub> micro-dendrites at 8 h. This coincides well with the inversely proportional relationship between crystallite size and narrowness of the XRD peaks (Fig. 2.14),

according to the Scherrer equation. Crystallinity, on the other hand (Fig. 2.14), was determined to evolve from the relatively amorphous (at 2 h), 90.8 (3 h), 91.1 (4 h), 91.2 (8 h), 92.2 (12 h), 92.0 (16 h), 92.0 (24 h) and 91.0 % (48 h), respectively. Unfortunately, we were not able to establish any obvious trend between crystallite (grain) size and crystallinity. Although sufficient *p*XRD data were also recorded for the Williamson-Hall plot, we did not find any useful correlation between the micro-strain effects and aging time of the crystal growth process based on information revealed by the crystalline lattices. Nevertheless, our time dependent measurements reveal no indication of any ferrihydrite, or intermediate phases formed. This agrees well with prior studies which suggest that  $\alpha$ -Fe<sub>2</sub>O<sub>3</sub> crystals were able to directly form due to the low saturation of Fe<sup>3+</sup> ions, as evident from the weak dissociation tendency of [Fe(CN)<sub>6</sub>]<sup>3-</sup> anions ( $K_{eq} = 1.0 \times 10^{42}$ ). Such reasoning supports the well-regarded diffusion-limited aggregation (DLA) hypothesis as the main explanation for the formation of these dendritic  $\alpha$ -Fe<sub>2</sub>O<sub>3</sub> micro-crystals.<sup>64</sup>

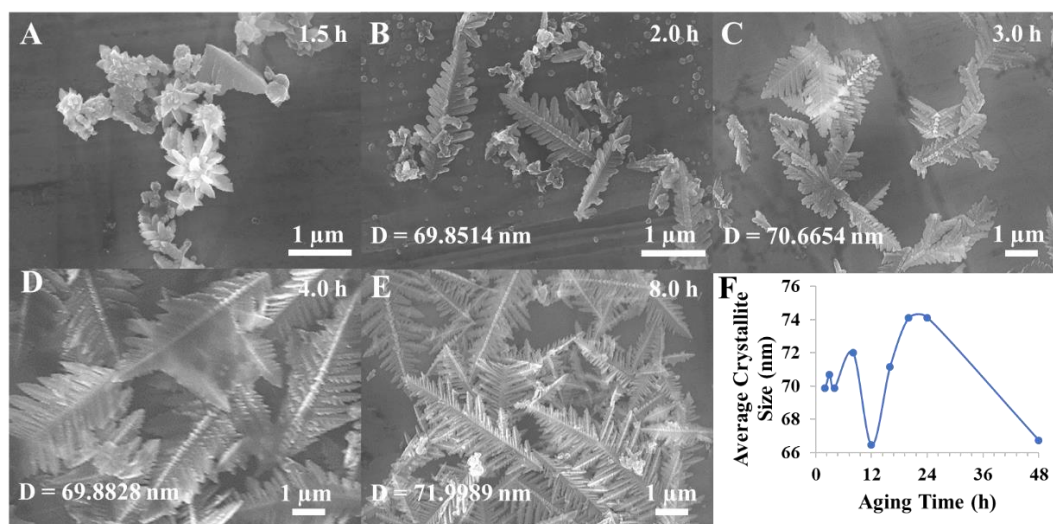


**Figure 2.13** High magnification SEM images of branched  $\alpha$ -Fe<sub>2</sub>O<sub>3</sub> structures synthesized with a K<sub>3</sub>[Fe(CN)<sub>6</sub>] concentration of 3.8 mM at 180°C for (A) 1.5, (B) 2.0, (C) 3.0, (D) 4.0 and (E) 8.0 h. (F) Average crystalline (grain) size “D” graph showing a typical crystal growth pattern with several dissolution-recrystallization cycles through the aging time.

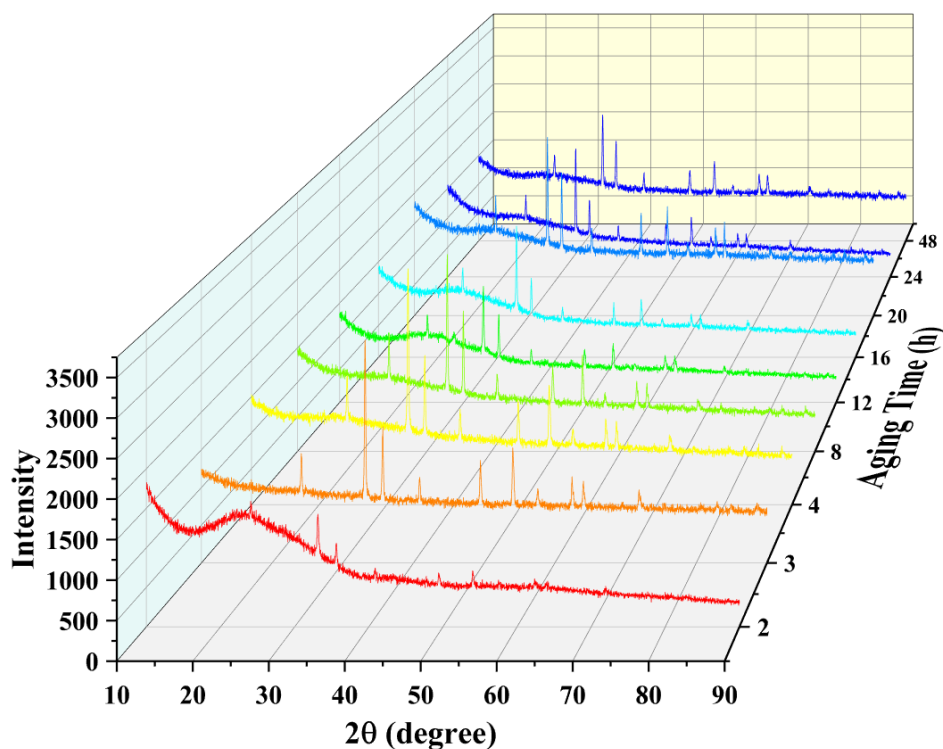


**Figure 2.14** Time-dependent *p*XRD patterns, showing the crystal growth (aging) process (from red to purple), of the typical branched  $\alpha$ -Fe<sub>2</sub>O<sub>3</sub> fractal structures synthesized with a K<sub>3</sub>[Fe(CN)<sub>6</sub>] concentration of 3.8 mM at 180°C from 2 to 48 h.

**Effect of H<sub>2</sub>O-to-EtOH & -DMF Volume Ratios.** To evaluate the morphological control due to solvent effects, we systematically varied the volume ratios between H<sub>2</sub>O-to-EtOH and -DMF. By reducing the H<sub>2</sub>O-to-EtOH ratio from (A) 3 : 1, (B) 1 : 1, and to (C) 1 : 3 (Fig. 2.15), we were able to show the morphological evolution from *tert*D2D to *hyp*B2D, then to the six-fold symmetric hexagonal micro-platelets (as described in Fig. 2.7 A). All the products consist of the as described pure  $\alpha$ -Fe<sub>2</sub>O<sub>3</sub> phase (Fig. 2.15 D). Crystallinity was determined to increase from 94.3, 96.5 and to 96.7 % as the volume ratio of H<sub>2</sub>O-to-EtOH decreases. Interestingly, this result is somewhat counter-intuitive as H<sub>2</sub>O is conventionally known to be crucial in the crystallization of most inorganic colloids.<sup>11</sup> Furthermore, the crystallite sizes were averaged to reveal a decreasing trend from 71, 66, and to 61 nm as the H<sub>2</sub>O-

to-EtOH ratio decreases. This calculated result agrees well with the observed hexagonal nano-platelets co-aligned to form the micron-sized hexagonal structures as previously described (Fig. 2.7 B).

With interest in the solvent effects of DMF, we further reduced the H<sub>2</sub>O-to-DMF volume ratios from (A) 1 : 0, (B) 3 : 1, (C) 1 : 1, and to (D) 1 : 3 (Fig. 2.16) to demonstrate the significance of DMF in the size reduction of dendritic micron-sized crystals. As depicted, the size distributions reveal the continual decrease in the primary 1° *stem*, secondary 2° *branch*, and tertiary 3° *leaflet* sizes (Fig. 2.16 E to G). Briefly, the 1° *stem* size, as the overall size, decreases from 4.6230, 2.3840, and to 1.3411 μm. Secondary 2° *branch* size decreases from 1.5459, 0.7878, and to 0.4831 μm. Tertiary 3° *leaflet* size decreases from 0.3026, 0.1519 and to 0.0970 μm as a consequence of decreasing H<sub>2</sub>O-to-DMF ratios from (A) 1 : 0 to (C) 1 : 1 (Fig. 2.16 A to C). Some of the size distributions, especially of 1° *stem*, seem to be of multi-modal nature. Note that any further in the reduction of the H<sub>2</sub>O-to-DMF volume ratio to 1 : 3 results in amorphous aggregates. Nonetheless, this proves the viability of our approach in synthesizing smaller *tertD3Ds*. Similarly, all the diffraction peaks (Fig. 2.16 H) were indexed to the pure α-Fe<sub>2</sub>O<sub>3</sub> phase. Crystallinity was calculated to decrease from (B) 99.5, (C) 96.0, and to (D) 86.9 % as the volume ratio of H<sub>2</sub>O-to-DMF decreases from 3 : 1 to 1 : 3 (Fig. 2.16 H). Contrary to the case of H<sub>2</sub>O-to-EtOH, H<sub>2</sub>O shows its significance here in contribution to the degree of crystallization for *tertD3Ds*. Moreover, the crystallite sizes were averaged to reveal a decreasing trend from 65, 53, and to 46 nm as H<sub>2</sub>O-to-DMF ratio decreases.

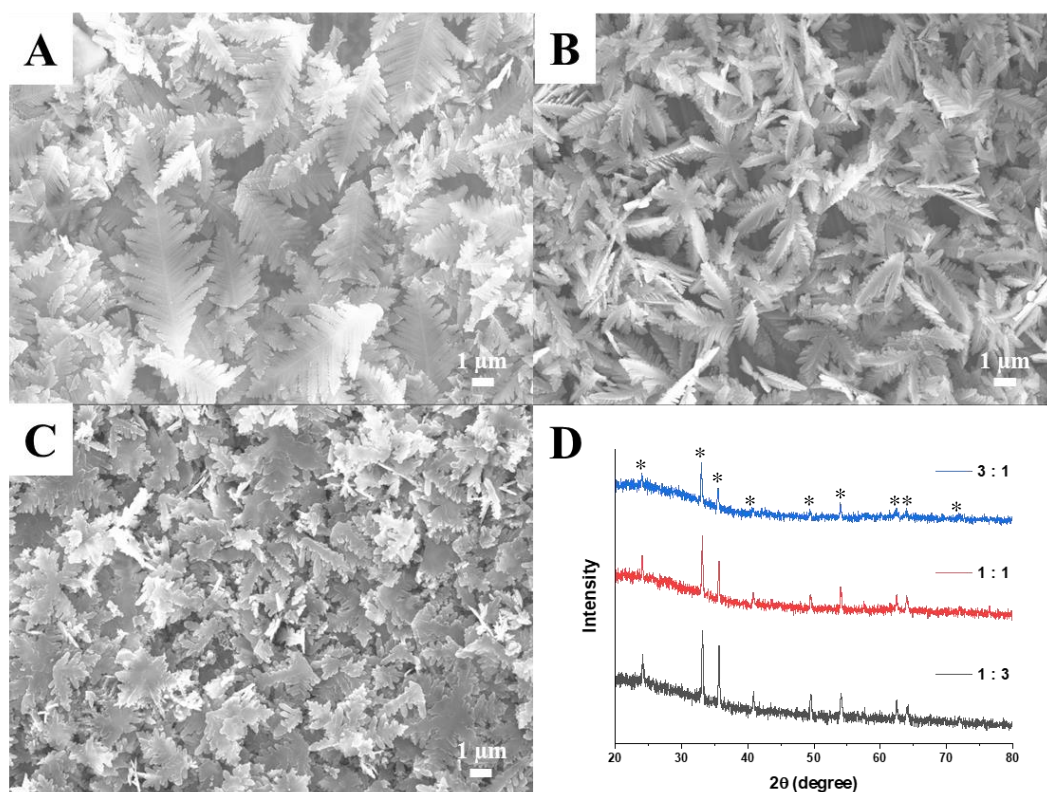


**Figure 2.15** Low magnification FE-SEM images of branched  $\alpha$ - $\text{Fe}_2\text{O}_3$  fractal structures synthesized with a  $\text{K}_3[\text{Fe}(\text{CN})_6]$  concentration of 4 mM at  $180^\circ\text{C}$  for 20 h in bi-solvent  $\text{H}_2\text{O}$ -to-EtOH volume ratios of (A) 3 : 1, (B) 1 : 1 and (C) 1 : 3. (D) *p*XRD pattern of the corresponding products synthesized under a variable mixture in  $\text{H}_2\text{O}$ :EtOH ratios, which are outlined as 3 : 1 (blue), 1 : 1 (red) and 1 : 3 (black), respectively.

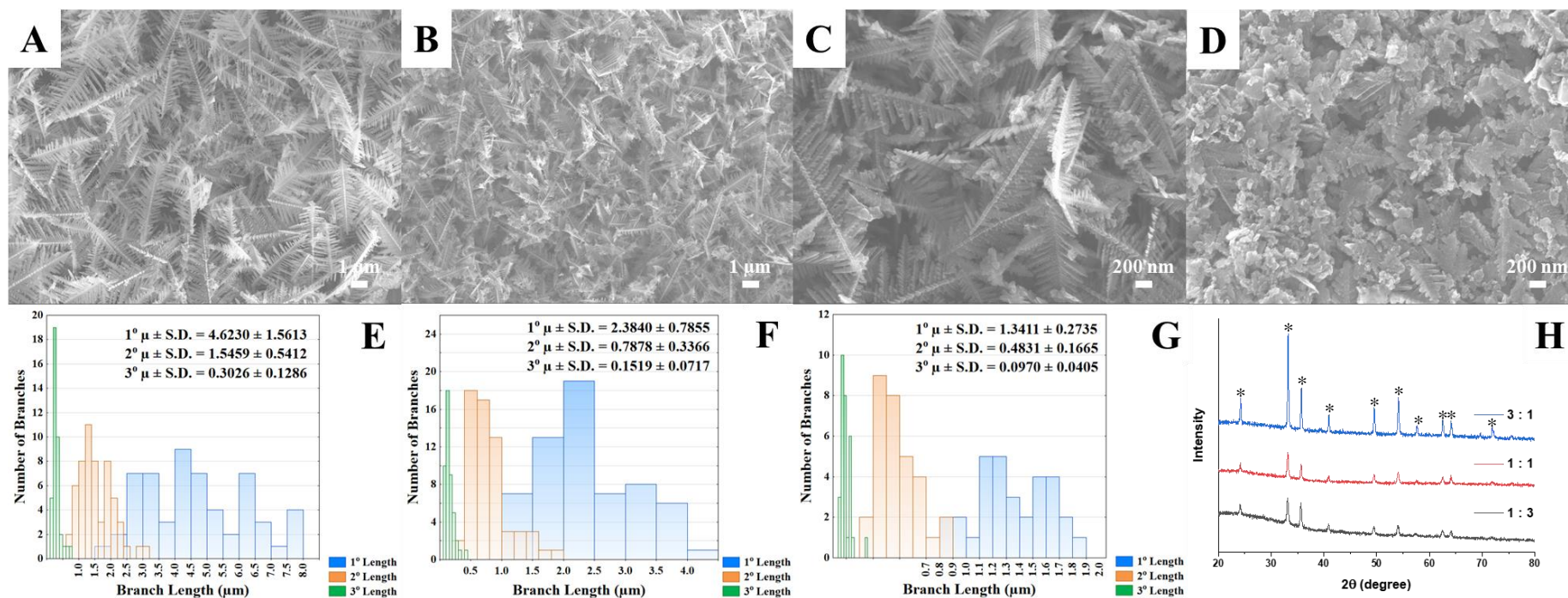


**Figure 2.16** Low magnification FE-SEM images of branched  $\alpha$ - $\text{Fe}_2\text{O}_3$  fractal structures synthesized with a  $\text{K}_3[\text{Fe}(\text{CN})_6]$  concentration of 4 mM at  $180^\circ\text{C}$  for 20 h in bi-solvent  $\text{H}_2\text{O}$ -to-DMF volume ratios of (A) 1 : 0, (B) 3 : 1, (C) 1 : 1 and (D) 1 : 3. (E-G) Size distribution data and (H) pXRD pattern of the corresponding products synthesized under a variable mixture in  $\text{H}_2\text{O}$ :DMF ratios, which are outlined as (E) 3 : 1 (blue), (F) 1 : 1 (red) and (G) 1 : 3 (black), respectively. The average “ $\mu$ ” lengths of primary 1° “stem” (blue), secondary 2° “branch” (orange) and tertiary 3° “leaflet” (green) structures, as calculated from individual measured particles with  $N = 60$  with an exception of (G) 1 : 3 where  $N = 30$ . Note: S.D. = Standard deviation calculated from a single variable, meaning  $N - 1$ .

**Photo-Fenton Oxidation of Azo-Type Textile Dyes.** To investigate the “structure-to-activity” relationships in the heterogeneous photo-Fenton catalysis, it is crucial to first establish some general criteria for our study. Prior photocatalytic studies have shown the importance of several variables regarding the *i*) overall size (which affects the specific surface area, relating to the number of exposed active sites), *ii*) morphology / shape (as in exposed facets), and *iii*) elemental (phase) composition. Collectively, all these factors contribute to the particle concentration, defined as the total number of particles per unit of volume. As the UV-Visible absorption of inorganic colloidal particles is highly morphology-dependent, we have measured and summarized the absorption spectra (*without normalization* in Fig. 2.17 A). It is interesting to note that *tert*D3Ds and *sec*S2Ds, possibly due to morphological differences, seem to possess a varied UV-Vis absorption trend. By applying the Tauc plot method, with  $\alpha h\nu = A_0(h\nu - E_g)^n$ , the bandgap energies ( $E_g$ ) of all the  $\alpha$ -Fe<sub>2</sub>O<sub>3</sub> crystalline solids as synthesized were extrapolated to be equal to 1.9 eV (assuming allowed indirect transitions,  $n = 2$ ), which deviates from the literature value of 2.1 eV for  $\alpha$ -Fe<sub>2</sub>O<sub>3</sub>. To evaluate the possibility of the dye-sensitized mechanism of photocatalysis, we also measured the UV-Vis absorption spectra (*not normalized*, Fig. 2.17 B) of Acid Red 26 (AR;  $\lambda_{\text{abs,max}} = 330 \text{ \& } 505 \text{ nm}$ ), Congo Red (CR;  $\lambda_{\text{abs,max}} = 346 \text{ \& } 498 \text{ nm}$ ), Chlorazol Black E (CB;  $\lambda_{\text{abs,max}} = 585 \text{ nm}$ ), Direct Blue 6 (DB;  $\lambda_{\text{abs,max}} = 585 \text{ nm}$ ), and Methyl Orange (MO;  $\lambda_{\text{abs,max}} = 465 \text{ nm}$ ), respectively. All these colorimetric dyes in this experiment are widely known as azo-type (-N=N-) dyes. During our experiments, CR was found to undergo gradual dark Fenton oxidation under exposure to H<sub>2</sub>O<sub>2</sub> as the oxidant. As a result, we did not examine the photo-degradation of CR. As AR was originally selected for the purpose of comparing with CR, due to its absorption, it was not examined as well.

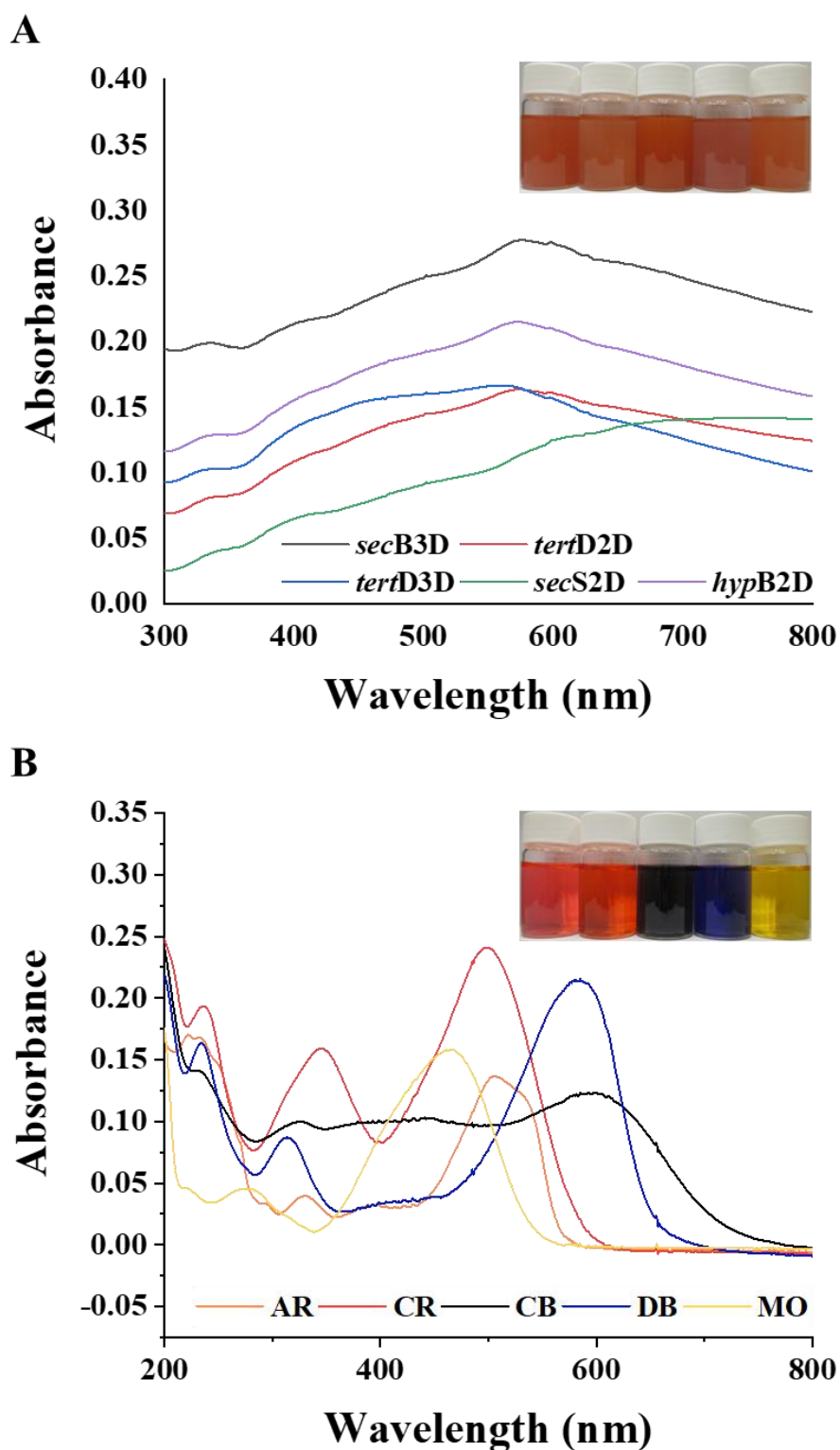


**Figure 2.17** UV-visible spectra of the (A) as synthesized branched  $\alpha$ -Fe<sub>2</sub>O<sub>3</sub> fractal structures, namely *secB3D* (black), *tertD2D* (red), *tertD3D* (blue), *secS2D* (green) and *hypB2D* (purple), dispersed at the concentration of 0.1 g/L in H<sub>2</sub>O (with an exception of *tertD3D* at 25 mg/L), and (B) azo-type textile dyes, namely AR (orange), CR (red), CB (black), DB (blue) and MO (yellow) dissolved at a concentration of 20  $\mu$ M in H<sub>2</sub>O.

To demonstrate the “structure-to-activity” relationship of all as-synthesized  $\alpha$ -Fe<sub>2</sub>O<sub>3</sub> micro-dendrites, we have carried out experiments for the photocatalytic degradation of CB, DB and MO in the presence of H<sub>2</sub>O<sub>2</sub>. To examine physio-adsorption, the adsorption-desorption equilibrium was first established via mild agitation. As shown, it seems that only *tert*D3Ds, *sec*S2Ds and *hyp*B2Ds adsorb CB (Fig. 2.18 D). The adsorbed CB (Ads, *first curve* in Fig. 2.18 A) shows the UV-Vis absorption after adsorption at the time when H<sub>2</sub>O<sub>2</sub> was added (*arrow* in Fig. 2.18 D) into the photocatalytic vial. The maximum absorbance of CB was measured and quantified at 585 nm. After 120 min of white light illumination, almost all of the CB dyes were photo-degraded. On contrary, only 5.7 % of CB was degraded under illumination without the photocatalyst (Fig. 2.19 A). Although both *tert*D3D and *hyp*B2D also showed a similar extent in the degradation, *sec*S2D featured the faster photocatalytic kinetics with CB decomposed at 28.3 (adsorbed), 35.0, 47.6, 81.4, and 99.9 % from 0 to 120 min (also highlighted by our representation in Fig. 2.18 A). Similarly, only *sec*B3Ds, *tert*D2Ds and *tert*D3Ds seem to adsorb DB well with varied extents (Fig. 2.18 E). The maximum absorbance of DB was quantified at 585 nm. Interestingly, *sec*B3Ds featured the fastest photo-degradation kinetics of DB from 12.1 (adsorbed), 45.2, 72.3 and 98.6 % from 0 to 60 min (Fig. 2.18 B). In comparison, only 3.4 % of DB (*blank*) was degraded under illumination at 60 min (Fig. 2.19 B). As for MO, similar extents of adsorption were found in all the as-synthesized dendritic  $\alpha$ -Fe<sub>2</sub>O<sub>3</sub> crystals (Fig. 2.18 F). The maximum absorbance of MO was quantified at 465 nm. Again, *sec*B3Ds featured the fastest photo-degradation kinetics of MO from 5.9 (adsorbed), 22.1, 33.2, 53.0, 80.3, 97.1 % and eventually to 100 % from 0 to 240 min (Fig. 2.18 C). In contrast, only 4.2 % of MO (*blank*) was degraded after sequential illumination for 240 min (Fig. 2.19 C).

Aside from the photo-Fenton degradation efficiency (%), as summarized (in Fig. 2.19 A to C), all the degradation experiments were also evaluated for the instantaneous rate constants. As H<sub>2</sub>O<sub>2</sub> was added in excess (of 10 mM as compared to 20 μM azo-type textile dyes), the pseudo-first order kinetics model was employed via the simple integral method. Most of the extrapolated lines were highly correlated ( $R^2 > 0.985$ ) (in Fig. 2.19 D to F) though there were a few exceptions (*lines not shown*; but with modest  $R^2 > 0.90$ ). The observed instantaneous rate constants for each degradation system were extrapolated and summarized (Table 2.1). Note that the degradation kinetics simply cannot be evaluated beyond the quantifiable period of time where incremental degradation differences were not observed. Nevertheless, the extrapolated pseudo-first order rate constants remain useful for comparison between our photocatalysts. As expected from prior discussion, *secS2D* was shown to degrade CB relatively quickly ( $k_{\text{instan.,obs.}}$  Of  $0.0231 \text{ s}^{-1}$ ), which is competitive to *secB3D* ( $k_{\text{instan.,obs.}}$  Of  $0.0212 \text{ s}^{-1}$ ) (Fig. 2.19 A and D). As for the photo-Fenton degradation of DB and MO, *secB3D* was found to perform the best among other photocatalysts with pseudo-first order rate constants ( $k_{\text{instan.,obs.}}$ ) of  $0.0385$  and  $0.0130 \text{ s}^{-1}$ , respectively.

Certainly, within the contemporary area of hierarchical photocatalysts, we humbly admit that many questions remain unexplored in our work. To mention a few, the dosage effect of the photocatalyst, azo-type dye and H<sub>2</sub>O<sub>2</sub> on the photocatalytic activity could be explored further. Moreover, the bulk pH should be measured at regular intervals of photo-Fenton oxidation for a more comprehensive study into the effect of pH. More interestingly, the concentration of bulk and surface hydroxyl radicals may be measured via established methods in the literature. With

consideration to environmental impact, the recyclability and stability of the dendritic  $\alpha\text{-Fe}_2\text{O}_3$  photocatalysts should also be evaluated. Importantly, as the complete mineralization of azo-type textile dyes is often unlikely, the resulting intermediates (derivatives) or by-products should be investigated.

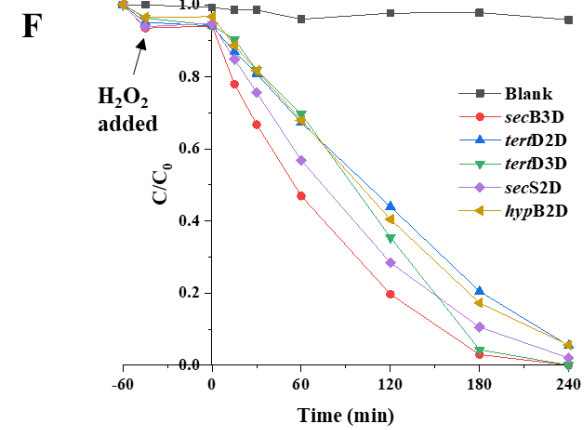
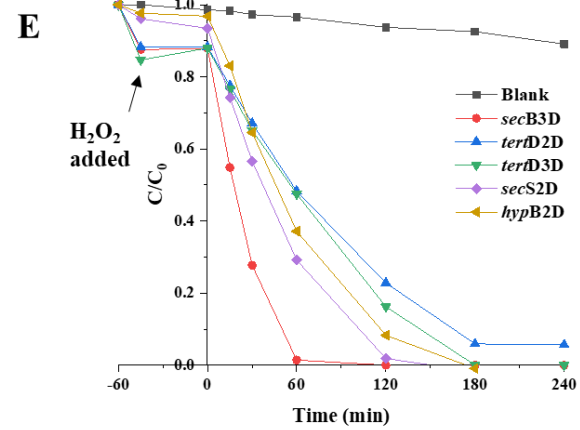
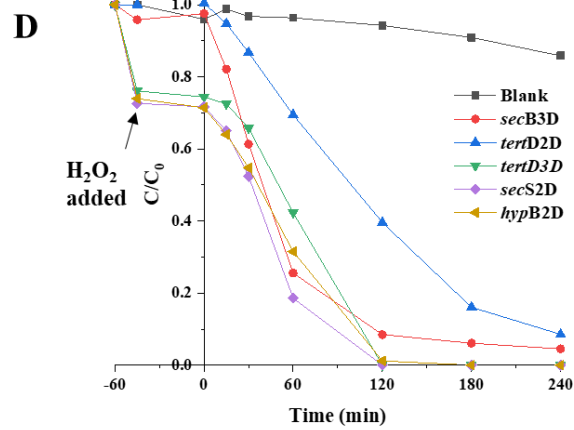
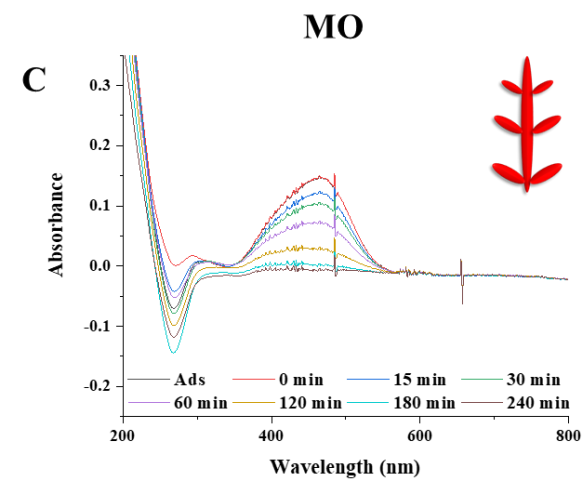
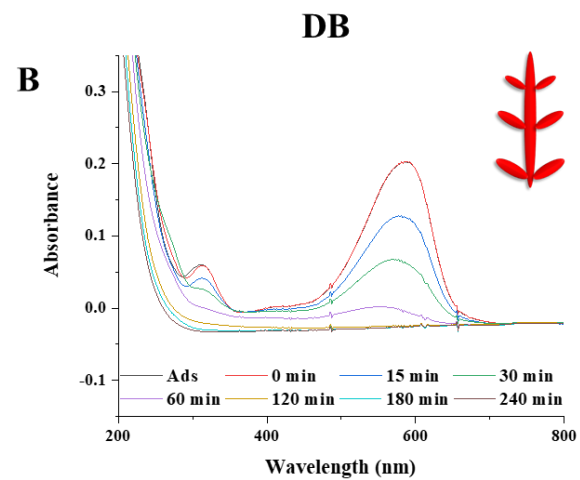
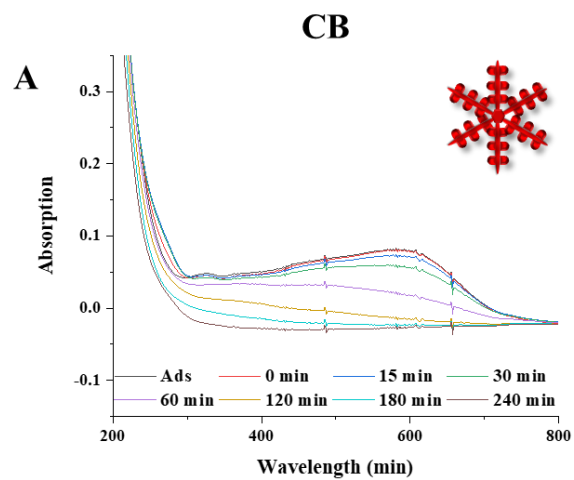


**Figure 2.18** UV-visible spectral changes of (A) CB, (B) DB and (C) MO as a function of irradiation time with H<sub>2</sub>O<sub>2</sub>, as the additive, in the presence of *sec*S2D and *sec*B3D (depicted in A and B,C). Photo-Fenton oxidation of (D) CB, (E) DB, and (F) MO upon exposure to all five distinctive  $\alpha$ -Fe<sub>2</sub>O<sub>3</sub> fractal structures under periodic visible (white) light illumination in the presence of H<sub>2</sub>O<sub>2</sub>. Conditions: Samples, namely *sec*B3D (—●—), *tert*D2D (—▲—), *tert*D3D (—▼—), *sec*S2D (—◆—) and *hyp*B2D (—◀—), at 0.1 g/L were dispersed with 20  $\mu$ M of the respective azo-type dye and 10 mM (0.0301 wt%) H<sub>2</sub>O<sub>2</sub> in a total of 15 mL aqueous solution under illumination of 5 W OLEDs (no cut-off filter), with an average light intensity of 148.5 mW cm<sup>-2</sup>, at the initial time of  $t = 0$  min. Prior to illumination, the adsorption-desorption equilibrium and any presence of the dark Fenton oxidation were first established and examined by  $t = -60, -45$  and 0 min. Blank (—■—) corresponds to the photo-degradation of azo-type dyes under illumination in the presence of H<sub>2</sub>O<sub>2</sub> only. C<sub>0</sub> and C symbolize the initial and final dye concentrations, which are measured at the maximum wavelength of absorbance “ $\lambda_{\text{abs,max}}$ ” before and after visible light irradiation, respectively.

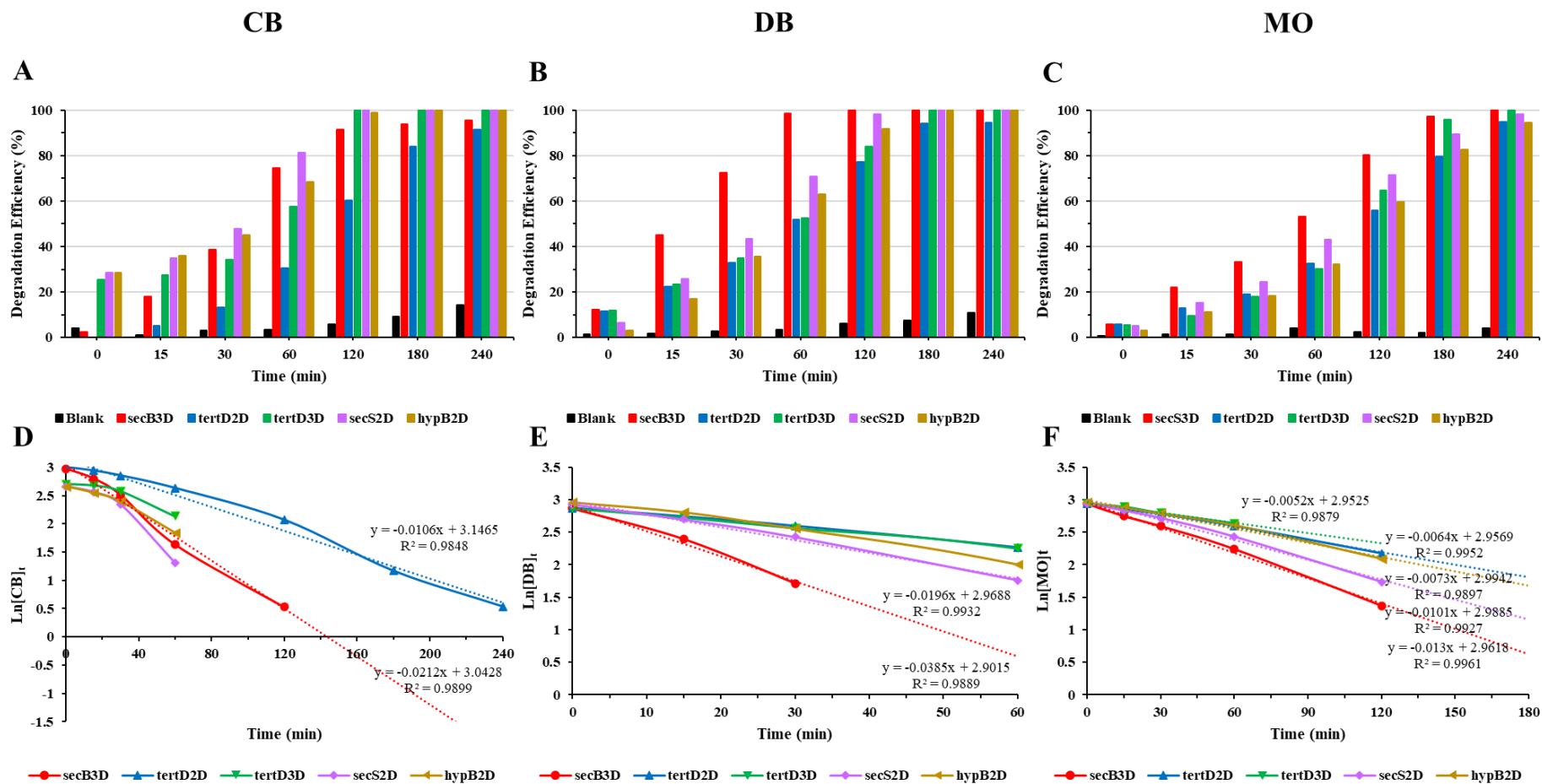


**Figure 2.19** Photo-Fenton degradation efficiency (%), as calculated by  $(1 - C/C_0) \times 100$ , of (A) CB, (B) DB and (C) MO as a function of irradiation time with H<sub>2</sub>O<sub>2</sub>, as the additive, in the presence of *blank* (black), *secB3D* (red), *tertD2D* (blue), *tertD3D* (green), *secS2D* (purple) and *hypB2D* (orange). Pseudo-first order kinetics of photo-Fenton oxidation of (D) CB, (E) DB, and (F) MO upon exposure to all five distinctive  $\alpha$ -Fe<sub>2</sub>O<sub>3</sub> fractal structures under periodic visible (white) light illumination in the presence of H<sub>2</sub>O<sub>2</sub>. Conditions: Samples, namely *secB3D* (—●—), *tertD2D* (—▲—), *tertD3D* (—▼—), *secS2D* (—◆—) and *hypB2D* (—◀—), at 0.1 g/L were dispersed with 20  $\mu$ M of the respective azo-type dye and 10 mM (0.0301 wt%) H<sub>2</sub>O<sub>2</sub> in a total of 15 mL aqueous solution under illumination of 5 W OLEDs (no cut-off filter), with an average light intensity of 148.5 mW cm<sup>-2</sup>, at the initial time of  $t = 0$  min. Blank (—■—) corresponds to the photo-degradation of azo-type dyes under illumination in the presence of H<sub>2</sub>O<sub>2</sub> only. C<sub>0</sub> and C symbolize the initial and final dye concentrations, which are measured at the maximum wavelength of absorbance “ $\lambda_{\text{abs,max}}$ ” before and after visible light irradiation, respectively.

**Table 2.1** Pseudo-first order rate constants of photo-Fenton oxidation of CB, DB, and MO upon exposure to all five distinctive  $\alpha$ -Fe<sub>2</sub>O<sub>3</sub> fractal structures under periodic visible (white) light illumination in the presence of H<sub>2</sub>O<sub>2</sub>. Conditions: Samples, namely *secB3D*, *tertD2D*, *tertD3D*, *secS2D* and *hypB2D*, at 0.1 g/L were dispersed with 20  $\mu$ M of the respective azo-type dye and 10 mM (0.0301 wt%) H<sub>2</sub>O<sub>2</sub> in a total of 15 mL aqueous solution under illumination of 5 W OLEDs (no cut-off filter), with an average light intensity of 148.5 mW cm<sup>-2</sup>, at the initial time of  $t = 0$  min.

$k_{\text{insta.,obs.}} (\text{s}^{-1})$	CB	DB	MO
<i>secB3D</i>	0.0212	0.0385	0.0130
<i>tertD2D</i>	0.0106	0.0114	0.0064
<i>tertD3D</i>	0.0098	0.0142	0.0052
<i>secS2D</i>	0.0231	0.0196	0.0101
<i>hypB2D</i>	0.0139	0.0209	0.0072

## 2.3 Experimental Procedure

**Materials.** Ultrapure H<sub>2</sub>O (18 mΩ·cm at 25°C; pH 7.4) was dispensed from a UV-equipped Synergy® water purification system (Merck Millipore). Potassium ferricyanide (III) (K<sub>3</sub>[Fe(CN)<sub>6</sub>], power or chunks < 10 μm, 99%) and Octylamine (99%) were purchased from Aldrich. Ethanol (EtOH, ≥ 99.5%) was purchased from VMR Chemicals. Dimethylformamide (DMF, min 99.8%) was purchased from RCI Labscan Limited. Ammonia (NH<sub>3</sub>, 32% GR) and 1-propanol (1-PrOH, GR 99.5+%) were both purchased from IL, USA. Methyl Orange (MO, Ind. Gr.) was purchased from Sinopharm Chemical Reagent Co. Ltd.. Acid Red 26 (AR), Congo Red (CR, > 98.0%) and Direct Blue 6 (DB) were all purchased from Tokyo Chemical Industry (TCI) Co. Ltd.. Chlorazol Black E (pure CB, certified) and Hydrogen Peroxide (35 wt.% solution in water, stabilized H<sub>2</sub>O<sub>2</sub>) were both purchased from Acros Organic. All materials were used as received.

**Solvothermal Synthesis of 2<sup>nd</sup> Generation Three-Dimensional (3D) α-Fe<sub>2</sub>O<sub>3</sub> Micro-Dendrites (*secB3D*).** The general procedures were adapted and slightly modified from previous protocols.<sup>67</sup> Briefly, prepare a mixture of H<sub>2</sub>O-to-EtOH in a 3 : 1 volumetric ratio in a 50-mL volumetric flask. Potassium ferricyanide (III) (0.0329 g, 0.1 mmol K<sub>3</sub>[Fe(CN)<sub>6</sub>]) was completely dissolved using the as prepared mixture into the 25-mL volumetric flask. The freshly prepared solution was immediately transferred into the 25-mL Teflon-lined autoclave with an occupancy of 80%. The Teflon-lined stainless steel autoclave was tightly sealed and immediately placed in a pre-heated air convection oven at 180°C for 20 h.

**Solvothermal Synthesis of 3<sup>rd</sup> Generation Two-Dimensional (2D) α-Fe<sub>2</sub>O<sub>3</sub> Micro-Dendrites (*tertD2D*).** Prior to mixing, potassium ferricyanide (III) (0.3292

g, 1 mmol  $\text{K}_3[\text{Fe}(\text{CN})_6]$ ) was first dissolved in a 25-mL volumetric flask followed by dilution for an aqueous stock concentration of 40 mM. The stock  $\text{K}_3[\text{Fe}(\text{CN})_6]$  solution was subsequently stored at 2°C and monitored via pH to ensure no significant change in the solution during storage. To induce re-precipitation, 10 mL of EtOH was first added into the 50-mL Teflon-lined autoclave. Subsequently, 4 mL of the as prepared 40 mM  $\text{K}_3[\text{Fe}(\text{CN})_6]$  stock solution was added. The precursor solution immediately turned milky yellow upon addition. Afterwards, 26 mL of  $\text{H}_2\text{O}$  was added dropwise without any swirling to induce re-dissolution for a clear yellow solution. The 50-mL Teflon-lined stainless steel autoclave was immediately sealed tightly and heated up gradually (20°C/min) in a forced air convection oven from 20 to 180°C. The tightly sealed autoclave was left at 180°C for 20 h.

**Solvothermal Synthesis of 3<sup>rd</sup> Generation Three-Dimensional (3D)  $\alpha\text{-Fe}_2\text{O}_3$  Micro-Dendrites (*tertD3D*).** Using the as prepared stock solution (mentioned above), 2 mL of the 40 mM  $\text{K}_3[\text{Fe}(\text{CN})_6]$  was added into the 25-mL Teflon-lined autoclave. Prior to mixing, 13 mL  $\text{H}_2\text{O}$  was added to dilute the precursor solution. Finally, 5 mL of DMF was added for a  $\text{H}_2\text{O}$ -to-DMF volumetric ratio of 3 : 1 with gentle swirling. The Teflon-lined stainless steel autoclave was sealed tightly and heated in a pre-heated air convection oven at 180°C for 20 h.

**Solvothermal Synthesis of Starfish-Like Two-Dimensional (2D)  $\alpha\text{-Fe}_2\text{O}_3$  Micro-Dendrites (*secS2D*).** To ensure basicity, 0.0214 wt.% (5.36 mM)  $\text{NH}_3$  was prepared by dispensing 16.7  $\mu\text{L}$   $\text{NH}_3$  (32 wt.%) into the 25-mL volumetric flask followed by dilution in  $\text{H}_2\text{O}$  up to the calibration mark. A 10 mL aliquot of the freshly prepared  $\text{NH}_4\text{OH}$  stock was first added into a typical 50-mL centrifuge tube. Subsequently, the  $\text{NH}_4\text{OH}$  stock solution was diluted with 4 mL  $\text{H}_2\text{O}$  and briefly

mixed via vortex mixing. To induce emulsion, 79.3  $\mu\text{L}$  of octylamine, as both the inhibitory ligand and reductant, was added and mixed into a cloudy solution. Furthermore, 3920.7  $\mu\text{L}$  1-PrOH was added to dissolve the octylamine accordingly with vortex mixing into a clear mixture. Lastly, 2 mL of the 40 mM  $\text{K}_3[\text{Fe}(\text{CN})_6]$  stock was added and mixed into a clear yellow mixture. As above, the Teflon-lined stainless steel autoclave was tightly sealed and placed in a pre-heated air convection oven at 180°C for 20 h.

**Solvothermal Synthesis of Hyper-Branched Two-Dimensional (2D)  $\alpha\text{-Fe}_2\text{O}_3$  Micro-Dendrites (*hypB2D*).** Firstly, add 1 mL of the as prepared 40 mM  $\text{K}_3[\text{Fe}(\text{CN})_6]$  stock into the 25-mL Teflon-lined autoclave. The stock solution was subsequently diluted with  $\text{H}_2\text{O}$  to 5 mL with swirling. Lastly, 5 mL EtOH was added with mild swirling to induce recrystallization. The Teflon-lined stainless steel autoclave, with a volume occupancy of 40%, was immediately sealed tightly and heated up gradually (20°C/min) in a forced air convection oven from 20 to 180°C. The tightly sealed autoclave was left at 180°C for 20 h.

**Purification of the As Synthesized  $\alpha\text{-Fe}_2\text{O}_3$  Micro-Dendrites.** The freshly heated Teflon-lined stainless steel autoclave was left to cool in the oven to a safe handling temperature of at least 80°C prior to leaving it out at ambient laboratory conditions. Once at room temperature, 50% of the supernatant from the top layer was extracted for the measurement of pH. Care was taken to ensure no impurities exist in the supernatant. Afterwards, the remaining 25% of the supernatant was extracted to remove any possible impurities on the surface. The remaining bright red precipitates settled at the bottom were rinsed with  $\text{H}_2\text{O}$  (5 mL x 3) thrice, and subsequently transferred into a specifically labelled 50-mL centrifuge tube. The isolated

precipitates were rinsed in H<sub>2</sub>O and EtOH (25 mL x 3) thrice consecutively in each solvent. Each rinsing was conducted in an ultrasound bath (45 kHz, *normal mode*) with a consecutive sequence of agitation and a complete revolution to emulate vortex mixing of the centrifuge tube in ultrasound. Each sequence was repeated thrice for around 12 secs each to obtain complete dispersion. Following each rinsing, the precipitates were isolated via centrifugation at 4,000 rpm for 10 mins. The as synthesized micron-sized  $\alpha$ -Fe<sub>2</sub>O<sub>3</sub> dendritic crystals were dried via vacuum through a Schlenk line for 12 h.

**Characterization.** X-ray diffraction (XRD) patterns were recorded with a Bruker D8 Advance X-Ray Diffractometer (XRD) equipped with a non-monochromated Cu K $\alpha$  radiation ( $\lambda = 1.5406 \text{ \AA}$ ). Diffraction patterns were collected from 20° to 80° at a rate of 1.0° per minute with a step size of 0.02°. The morphology of the products was characterized by field-emission scanning electron microscopy (FESEM, LEO 1530) equipped with an energy-dispersive X-ray (EDX, Oxford) spectrometer. Copper tape was attached to individual sample stubs for the deposition of dispersed ethanolic solutions of the samples (~ 0.5 g/L) via drop-casting and subsequent drying with the light tapping of a cut-off Whatman filter paper along the edges of the tape. Accurate sizes were measured by Tecnai G2 20 S-TWIN Transmission Electron Microscope (TEM) operating at 200 kV. Samples were deposited on thin amorphous carbon films supported by copper grids (mesh 200) from the dispersed ethanolic solutions (~ 0.1 g/L) of the products. Thermogravimetric analyses were conducted by a Perkin Elmer thermal gravimetric analyzer (TGA) with programmable temperature range from 40 to 900°C. The programmable settings were as follows: with *i*) holding for 1 min at 40°C, *ii*) heating from 40 to 900°C at

40°C/min, and *iii*) holding for 1 min at 900°C. Fourier transform infrared (FTIR) spectra were recorded by the PerkinElmer FT-IR Spectrum Two system equipped with an ATR detector. Ultraviolet-visible (UV-Vis) spectra were recorded using Agilent Cary 8454 UV-Vis spectrophotometer equipped with a diode array system.

**Photo-Fenton Catalysis Evaluation.** The photocatalytic activity of the hematite ( $\alpha$ -Fe<sub>2</sub>O<sub>3</sub>) dendritic crystals was determined by performing the degradation of Chlorazol Black E (CB), Direct Blue 6 (DB) and Methyl Orange (MO) in aqueous solution. For preparation, 10 mg of the  $\alpha$ -Fe<sub>2</sub>O<sub>3</sub> particle samples was first dispersed in 10 mL of H<sub>2</sub>O via ultrasound for a particle concentration of 1 g/L. For dilution, 12.5 mL of H<sub>2</sub>O was first added into the 15 mL Pyrex glass vial. Afterwards, 1 mL of the 300  $\mu$ M azo-type dye stock was added into the vial. Subsequently, 1.5 mL of the particle solution (1 g/L) was added. The suspension was mildly swirled in the dark for 15 mins to reach the adsorption-desorption equilibrium, followed by the addition of 12.9  $\mu$ L of hydrogen peroxide (35 wt.% H<sub>2</sub>O<sub>2</sub>, stabilized). Similarly, the mixture was mildly swirled in the dark for 45 mins to ensure the absence of dark Fenton oxidation. To induce photo-Fenton, the suspension was illuminated by a multichannel photochemical reaction system (5 W  $\times$  9 slots) fixed with OLED white light (PCX50B, 148.5 mW/cm<sup>2</sup>) as the light source. No cut-off filter was used during photo-degradation. However, Pyrex glass is known for absorbing at the UV light (< 350 nm), thus blocking some light to the solution. During operation, the samples were mechanically swirled at 100 rpm and air-cooled continuously by the photochemical reactor to maintain room temperature. At regular intervals, an aliquot of 1.5 mL was sampled and centrifuged to separate the textile dye from the particles in suspension to be measured by means of the UV/vis spectrophotometer.

The characteristic wavelengths of CB, DB and MO were 585, 585 and 465 nm, respectively.

## 2.4 Summary & Future Work

Structure-activity relationship (SAR) of three-dimensional macromolecules, especially for proteins, has been a prevalent topic among chemists, biochemists, and computational chemists for more than two decades. Crystal structures with defined geometric restrictions of the lattice and motif provide the basis to study SARs. Given the repertoire of crystalline morphologies available in the literature at the nano- and micro-scale, the colloidal synthesis allows an avid experimentalist to explore the SARs, which is commonly known as “facet-dependent” properties in colloidal crystals for different applications, such as in heterogeneous photocatalysis.

In our study, we examined the photocatalytic Fenton oxidation of azo-type dyes, which are chlorazol black E (CB), direct blue 6 (DB) and methyl orange (MO), in the presence of the optimized dendritic or branched  $\alpha$ -Fe<sub>2</sub>O<sub>3</sub> micro-crystals. We have found that the conventional *sec*B3Ds with favourable facets of {10-10} remain superior in the photocatalytic degradation of DB and MO with pseudo-first order rate constants ( $k_{\text{insta.,obs.}}$ ) of 0.0385 and 0.0130 s<sup>-1</sup>, respectively. Interestingly, *sec*S2Ds with {11-20} was discovered to photo-degrade sufficiently well, as compared to other synthesized photocatalysts, in the presence of CB ( $k_{\text{insta.,obs.}}$  of 0.0231 s<sup>-1</sup>), a highly absorbing azo-type dye.

We encourage and recommend future contender or on-lookers to explore their own step-by-step synthesis towards prospective applications. Future work, although mentioned in our last discussion, should be proceeded with caution according to the contemporary or state-of-the-art in one’s own research field.

## Reference

1. Curtis P. Schuh, *Mineralogy & Crystallography: An Annotated Bibliography of Books* published 1469 through 1919.
2. M.; Werner, *Crystal Structure Determination*, Springer-Verlag Berlin Heidelberg, 2004.
3. Buck, M. R.; Schaak, R. E. *Angew. Chemie Int. Ed.* **2013**, 52 (24), 6154–6178.
4. Hayes, S. M.; McCullough, E. A. *Resource Policy* **2018**, 59, 192–199.
5. R. M.; Cornell, U.; Schwertmann, *The Iron Oxides: Structure Properties, Reactions, Occurrences and Uses*, Wiley-VCH, 2006.
6. D.; Faivre, R. B.; Frankel, *Iron Oxides: From Nature to Applications*, Wiley-VCH, 2016.
7. Hench, L. L.; West, J. K. *Chem. Rev.* **1990**, 90, 33–72.
8. Hagemans, F.; Pujala, R. K.; Hotie, D. S.; Thies-weesie, D. M. E.; Winter, D. A. M. De; Meeldijk, J. D.; Blaaderen, A. Van; Imhof, A. *Chem. Mater.* **2018**. (*in press*)
9. Jolivet, J.-P.; Chanéac, C.; Tronc, E. *Chem. Commun.* **2004**, No. 5, 477–483.
10. Hamada, S.; Matijevic, E. *J. Colloidal and Interface Sci.* **1981**, 84 (1).
11. Ozaki, M.; Kratochvil, S.; Matijevic. E. *J. Colloidal and Interface Sci.* **1984**, 102 (1), 146.
12. Rao, X.; Su, X.; Yang, C.; Wang, J.; Zhen, X.; Ling, D. *CrystEngComm* **2013**, 15 (36), 7250.
13. Erbs, J. J.; Gilbert, B.; Penn, R. L. *J. Phys. Chem. C* **2008**, 112 (32), 12127–12133.
14. Asenath-Smith, E.; Estroff, L. A. *Cryst. Growth Des.* **2015**, 15 (7), 3388–3398.

15. Das, S.; Hendry, M. J.; Essilfie-Dughan, J. *Environ. Sci. Technol.* **2011**, *45* (1), 268–275.
16. Lanzl, C. A.; Baltrusaitis, J.; Cwiertny, D. M. *Langmuir* **2012**, *28* (45), 15797–15808.
17. Liu, Z.; Lv, B.; Wu, D.; Zhu, Y.; Sun, Y. *CrystEngComm* **2012**, *14* (11), 4074.
18. Feld, A.; Weimer, A.; Kornowski, A.; Winckelmans, N.; Merkl, J.; Kloust, H.; Zierold, R.; Schmidtke, C.; Schotten, T.; Riedner, M.; Bals, S. *ACS Nano*. **2018**. (*in press*)
19. Cozzoli, P. D.; Snoeck, E.; Garcia, M. A.; Giannini, C.; Guagliardi, A.; Cervellino, A.; Gozzo, F.; Hernando, A.; Achterhold, K.; Ciobanu, N.; Parak, F. G.; Cingolani, R.; Manna, L. *Nano Lett.* **2006**, *6* (9), 1966–1972.
20. Wang, X.; Qiu, J.; Qu, J.; Wang, Z.; Su, D. *RSC Adv.* **2012**, *2* (10), 4329–4334.
21. Zhao, Z.; Zhou, Z.; Bao, J.; Wang, Z.; Hu, J.; Chi, X.; Ni, K.; Wang, R.; Chen, X.; Chen, Z.; Gao, J. *Nat. Commun.* **2013**, *4*, 1–7.
22. Cao, M.; Liu, T.; Gao, S.; Sun, G.; Wu, X.; Hu, C.; Zhong, L. W.; Wang, Z. L. *Angew. Chemie - Int. Ed.* **2005**, *44* (27), 4197–4201.
23. Wang, S.-B.; Min, Y.-L.; Yu, S.-H. *J. Phys. Chem. C* **2007**, *111* (9), 3551–3554.
24. Jia, B.; Gao, L. *Cryst. Growth Des.* **2008**, *8* (4), 1372–1376.
25. Rodriguez, R. D.; Demaille, D.; Lacaze, E.; Jupille, J.; Chaneac, C.; Jolivet, J.-P. *J. Phys. Chem. C* **2007**, *111* (45), 16866–16870.
26. Kim, C. W.; Kang, M. J.; Van, T. K.; Kang, Y. S. *J. Ind. Eng. Chem.* **2017**, *53*, 341–347.
27. Liu, R.; Jiang, Y.; Fan, H.; Lu, Q.; Du, W.; Gao, F. *Chem. - A Eur. J.* **2012**, *18* (29), 8957–8963.

28. Ouyang, J.; Pei, J.; Kuang, Q.; Xie, Z.; Zheng, L. *ACS Appl. Mater. Interfaces* **2014**, *6* (15), 12505–12514.
29. Cha, H. G.; Nguyen, C. K.; Kim, S.; Jung, M.; Kang, Y. S. *Cryst. Growth Des.* **2012**, *12*, 862–868.
30. Kim, C. W.; Kang, M. J.; Van, T. K.; Kang, Y. S. *J. Ind. Eng. Chem.* **2017**, *53*, 341–347.
31. Lv, B.; Liu, Z.; Tian, H.; Xu, Y.; Wu, D.; Sun, Y. *Adv. Funct. Mater.* **2010**, *20* (22), 3987–3996.
32. Lin, M.; Tng, L.; Lim, T.; Choo, M.; Zhang, J.; Tan, H. R.; Bai, S. *J. Phys. Chem. C* **2014**, *118* (20), 10903–10910.
33. Li, Z.; Lai, X.; Wang, H.; Mao, D.; Xing, C.; Wang, D. *Nanotechnology* **2009**, *20* (24), 25603–25612.
34. Jia, C.-J.; Sun, L.-D.; Yan, Z.-G.; You, L.-P.; Luo, F.; Han, X.-D.; Pang, Y.-C.; Zhang, Z.; Yan, C.-H. *Angew. Chemie Int. Ed.* **2005**, *44* (28), 4328–4333.
35. Thanh, N. T. K.; Maclean, N.; Mahiddine, S. *Chem. Rev.* **2014**, *114* (15), 7610–7630.
36. Fuguet, E.; Clara, R.; Bosch, E. *Analytica Chimica Acta* **2005**, *548*, 95–100.
37. Klunker, M.; Tahir, M. N.; Dören, R.; Deuker, M.; Komforth, P.; Plana-Ruiz, S.; Barton, B.; Shylin, S. I.; Ksenofontov, V.; Panthöfer, M.; Wiesmann, N.; Herzberger, J.; Möller, A.; Frey, H.; Brieger, J.; Kolb, U.; Tremel, W. *Chem. Mater.* **2018**, *30* (13), 4277–4288.
38. Niu, M.; Huang, F.; Cui, L.; Huang, P.; Yu, Y.; Wang, Y. *ACS Nano* **2010**, *4* (2), 681–688.
39. Mullin, J. W. *In Crystallization*; Mullin, J. W., Ed.; Butterworth-Heinemann:

Boston, 1997.

40. Green, A. E.; Chiang, C. Y.; Greer, H. F.; Waller, A.; Ruszin, A.; Webster, J.; Niu, Z.; Self, K.; Zhou, W. *Cryst. Growth Des.* **2017**, *17* (2), 800–808.
41. Zepp, R.; Faust, B. C.; Hoigne, J. *Environ. Sci. Technol.* **1992**, *26* (2), 313–319.
42. Kwan, W. P.; Voelker, B. M. *Environ. Sci. Technol.* **2003**, *37*, 1150–1158.
43. Chen, L.; Ma, J.; Li, X.; Zhang, J.; Fang, J.; Guan, J.; Xie, P. *Environ. Sci. Technol.* **2011**, *45*, 3925–3930.
44. Xu, L.; Wang, J. *Environ. Sci. Technol.* **2012**, *46*, 10145–10153.
45. Sun, M.; Chu, C.; Geng, F.; Lu, X.; Qu, J.; Crittenden, J.; Elimelech, M.; Kim, J.-H. *Environ. Sci. Technol. Lett.* **2018**, *5*, 186–191.
46. Natarajan, S.; Bajaj, H.; Tayade, R. *J. of Environ. Sci.* **2018**, *65*, 201–222.
47. Luo, W.; Zhu, L.; Wang, N.; Tang, H.; Cao, M.; She, Y. *Environ. Sci. Technol.* **2010**, *44*, 1786–1791.
48. Bharathi, S.; Nataraj, D.; Seetha, M.; Mangalaraj, D.; Ponpandian, N.; Masuda, Y.; Senthil, K.; Yong, K. *CrystEngComm* **2010**, *12*, 373–382.
49. Esen, C.; Schweiger, G. *J. Colloid Interface Sci.* **1996**, *179*, 276–280.
50. Gu, J.; Li, S.; Wang, E.; Li, Q.; Sun, G.; Xu, R.; Zhang, H. *J. Solid State Chem.* **2009**, *182*, 1265–1272.
51. Liu, Z.; Chiang, C.-Y.; Li, W.; Zhou, W. *Chem. Commun.* **2015**, *51*, 9350.
52. Zhang, X.; Sui, C.; Gong, J.; Su, Z.; Qu, L. *J. Phys. Chem. C* **2007**, *111*, 9049–9054.
53. Cai, X.; Lin, J.; Pang, M. *Cryst. Growth Des.* **2016**, *16* (7), 3565–3568.
54. Thøron, C.; Gallud, A.; Carcel, C.; Gary-bobo, M.; Maynadier, M.; Garcia, M.;

- Lu, J.; Tamanoi, F.; Zink, J. I.; Wong, M.; Man, C. *Chem. Eur. J.* **2014**, *20*, 9372–9380.
55. Witten, T. A.; Sander, L. M. *Phys. Rev. Lett.* **1981**, *47*, 1400–1403.
56. Penn, R. L.; Soltis, J. A. *CrystEngComm* **2014**, *16*, 1409.
57. Gebauer, D.; Kellermeier, M.; Gale, J. D.; Bergström, L.; Cölfen, H. *Chem. Soc. Rev.* **2014**, *43* (7), 2348–2371.
58. Pastorizo-Santos, I.; Liz-Marzán, L. M. *Adv. Funct. Mater.* **2009**, *19* (5), 679–688.
59. Chowdhury, M.; Fester, V.; Kale, G. *J. Cryst. Growth* **2014**, *387*, 57–65.
60. Shtukenberg, A. G.; Punin, Y. O.; Gunn, E.; Kahr, B. *Chem. Rev.* **2012**, *112* (3), 1805–1838.
61. Shen, D.; Yang, J.; Li, X.; Zhou, L.; Zhang, R.; Li, W.; Chen, L.; Wang, R.; Zhang, F.; Zhao, D. *Nano Lett.* **2014**, *14* (2), 923–932.
62. Leung, K. C.; Xuan, S.; Wang, F.; Gong, X.; Kong, S.; Yu, C. *Chem. Commun.* **2011**, *47* (9), 2514–6.
63. Jiao, Y.; Liu, Y.; Qu, F.; Wu, X. *CrystEngComm* **2014**, *16* (4), 575–580.
64. Barrón, V.; Torrent, J. *J. Colloid Interface Sci.* **1996**, *177*, 407–410.
65. Chen, L.; Yang, X.; Chen, J.; Liu, J.; Wu, H.; Z., H.; Liang, C.; Wu, M. *Inorg. Chem.* **2010**, *49*, 8410–8420.

# **CURRICULUM VITAE**

Academic qualifications of the thesis author, Mr. LAI Joshua:

- Received the degree of Bachelor of Science from McGill University, June 2014.
- Received the degree of Master of Science from Technical University of Munich and National University of Singapore, April 2017.

October 2020